UNIVERSIDADE Đ
COIMBRA

Ana João Rodrigues da Fonseca

CHEMISTRY VS TOPOGRAPHY:
INFLUENCE ON THE BIOTIC INTERFACE

Dissertação de Mestrado Integrado em Engenharia Biomédica,
especialização em Instrumentação Médica e Biomateriais,
orientada pela Professora Doutora Ana Paula da Fonseca Piedade
e apresentada ao Departamento de Engenharia Mecânica
da Faculdade de Ciências e Tecnologia da Universidade de Coimbra

Setembro de 2018

UNIVERSIDADE D COIMBRA

FACULDADE
DE CIÊNCIAS
E TECNOLOGIA

Ana João Rodrigues da Fonseca

Chemistry vs Topography: Influence on the biotic interface

Thesis submitted to the
University of Coimbra for the degree of
Master in Biomedical Engineering

Supervisor:
Ana Paula da Fonseca Piedade

Coimbra, 2018

This work was developped within the frame of the Add.additive project (POCI-01-0247-FEDER-024533):

COMPETE 2020
PORTUGAL 2020
UNIÃO EUROPEIA
Fundos Europeus Estruturais e de Investimento

Esta cópia da tese é fornecida na condição de que quem a consulta reconhece que os direitos de autor são pertença do autor da tese e que nenhuma citação ou informação obtida a partir dela pode ser publicada sem a referência apropriada.

This copy of the thesis has been supplied on condition that anyone who consults it is understood to recognize that its copyright rests with its author and that no quotation from the thesis and no information derived from it may be published without proper acknowledgement.

”Nothing in life is to be feared, it is only to be understood. Now is the time to understand more, so that we may fear less.”

Marie Curie

To my parents.

Acknowledgments

First, I want to express my gratitude to my supervisor, Doctor Ana Paula Piedade, for providing me all the guidance needed for this project, for always being available and willing to help me throughout this past year. Her good disposition and accessibility made this whole experience a great pleasure.

I want to acknowledge the Add.Additive Project - add additive manufacturing to Portuguese industry (POCI-01-0247-FEDER-024533) - for funding this project.

I would like to thank Doctor Teresa Vieira for receiving me in the group of Materials and Surface Engineering, making the work developed in this dissertation possible.

I am grateful for all the help and availability provided by Doctor Pedro Antunes, from the Department of Mechanical Engineering of the University of Coimbra, on the execution of the mechanical tests.

I want to thank Doctor Ana Colette Maurício, from the Abel Salazar Institute of Biomedical Sciences (ICBAS), for making possible the realization of the *in vitro* tests, for the availability to receive me and the time spent in this project.

I also want to acknowledge Doctor Mahmoud Tavakoli, from the Institute of Systems and Robotics of the University of Coimbra, for providing the PDMS used in this work.

A sincere thanks to Doctor Theo van Kooten for the enthusiasm with which he lectured the Interface Biology course, in Groningen, and for have awakened in me the interest in this field. I truly appreciate the willingness he had to receive me.

To my parents, I will be forever grateful for everything they have allowed me to do in my life. For all the unconditional love and support they have gave me, not only this year, but through all of my life. For all the freedom they have provide me and for never expecting nothing from me but my best. Thank you for making me the person I am. I see you in me more and more each day.

To my family, I deeply appreciate all the words of encouragement and all the warmth. I know that I can always count on them. A special thanks to Daniela and Verónica, for always being there for me, for all the laughs and moments we shared.

You will always be the sisters I have never had.

A sincere thank you to my friends from Coimbra, Inês, Ana Luísa, Gonçalo, Ricardo, João Miguel, Pedro, João Pedro e Filipa. For all the moments we shared throughout these 5 years. For all the laughter and for being my support away from home. I will take you with me forever in my heart.

To my friend Sofia, I am grateful for her friendship and for always believing in me.

And finally, a special thanks to my Erasmus friends, for making me see that life is not meant to be taken so seriously.

To all of you, I am deeply grateful.

Abstract

The biological environment in which cells reside *in vivo* is highly organized from the nano- to the micro- and macroscale. Over the past decades, it has been demonstrated that cells can sense and respond to their microenvironment, especially to physical stimuli and chemical signals. Among the physical cues, surface topography and stiffness have shown to strongly influence cell behavior.

This dissertation had the main purpose of modifying the chemistry and topography of poly(dimethylsiloxane) (PDMS) substrates through the deposition of thin films by magnetron sputtering and test *in vitro* the surfaces obtained to conclude on cellular behavior.

Thin films of poly(tetrafluoroethylene) (PTFE) and polyamide (PA) were deposited onto previously strained PDMS substrates. Ordered wrinkling patterns were obtained at the microscale, as well as nanometric roughness. The films created were chemically, physically and mechanically characterized and mechanical tests were performed. The wrinkles remained after cyclic straining the samples. Finally, the samples were tested *in vitro* with human umbilical cord mesenchymal stem cells (hUC-MSCs). Cells were able to adhere, proliferate and differentiate on the PTFE and PA modified PDMS. Furthermore, cell alignment was induced by the films wrinkled topography.

The work developed in this project has the potential to be used in many biomedical applications for cell culture, cell detection/screening, implantation, tissue engineering, microfluidics and biosensors.

Keywords:
RF magnetron sputtering; poly(dimethylsiloxane); poly(tetrafluoroethylene);
polyamide; wrinkled topography; human umbilical cord mesenchymal stem cells.

List of Figures

1.1 Molecular architecture of focal contacts [25]. 4

1.2 Surface modification methods. Adapted from [19]. 5

1.3 Scheme of the adsorption of an adhesion protein to (A) a hydrophobic material surface and (B) a hydrophilic surface [6]. 7

1.4 Schematics of surface topographic patterns commonly used as cell culture substrates [7] 12

1.5 (a) Scheme of a wrinkled surface pattern. (b and c) Optical micrographs of PDMS substrates of different thicknesses after PTFE thin film deposition, resulting in aligned distribution in (b) and random displacement in (c) (current work). 13

1.6 Schematic representation of wrinkle formation in a structure composed of two layers [57]. 15

1.7 Scheme of a magnetron sputter device. Adapted from [61]. 16

2.1 Alicona Infinite Focus Light Microscope. Scheme of form and roughness measurements [66]. 23

2.2 Schematic of dynamic AFM mode operation [69]. 24

2.3 Scheme of a scanning electron microscope [72]. 25

2.4 Contact angle of a sessile drop. 27

2.5 Schematic of advancing and receding contact angles [79]. 27

2.6 Schematic representation of the Wenzel model. 28

2.7 Schematic representation of the Cassie and Baxter model. 28

2.8 Representation of the double layered developed on a particle suspended in a dispersion medium [84]. 30

2.9 Representation of (a) stress applied to a material over time and the strain response in case of (b) an elastic material, (c) viscous fluid or (d) viscoelastic material. Adapted from [85]. 31

2.10 Stress-strain curve obtained from a tensile test [86]. 32

2.11 Autograph AGS-1kNX model from Shimadzu. Photo taken during the tensile tests. 32
2.12 Typical stress response of a viscoelastic material to the stress-relaxation test [89]. 33
2.13 Typical stress response of a viscoelastic material to the cyclic test [89]. 34

3.1 Optical micrographs of PTFE deposited thin films onto PDMS: (a) 100 μm thick PDMS sample; (b) 400 μm thick PDMS without previous deformation, (c) 1000 μm thick PDMS without previous deformation; (d) 400 μm thick PDMS with 10% previous deformation; (e) the 400 μm thick PDMS with 15% previous deformation. 40
3.2 Schematic representation of the approach followed to create transversal and longitudinal wrinkling patterns on the PDMS surface. 41
3.3 Optical micrographs of the PDMS substrates after the deposition of: (a, b) a PTFE thin film; (c, d) PA thin film. 42
3.4 IFM analysis of AJ_6 thin film. Representation of the 2D roughness profile for wavelength and amplitude evaluation (b) from the position indicated by the red line in (a). 43
3.5 SEM micrographs of the PTFE film (a, b, c) and the film PA (d, e) deposited onto the PDMS substrates. 45
3.6 Topographic (a) and phase (b) images of the PTFE film deposited over silicon. 46
3.7 Topographic (a) and phase (b) images of the PA film deposited over silicon. 46
3.8 Model of fluorocarbon plasma polymer obtained by PTFE sputtering (the black dots represent carbon atoms and the white dots represent fluorine atoms). Adapted from [94]. 47
3.9 Diffractograms of the PTFE target and the PTFE thin film deposited onto glass. The same observation, due to the same reasons, was observed for the PA deposited thin film. 47
3.10 IR absorption spectrum of the PTFE target (upper figure) and the film resulting from its deposition on the silicon substrate (lower figure). 49
3.11 IR absorption spectrum of the PA target (upper figure) and the film resulting from its deposition on the silicon substrate (lower figure). . . 50
3.12 Contact angle variance with time for the PA film on PDMS. 52
3.13 Stress-strain curves of the tensile tests performed for PTFE and PA modified PDMS and unmodified PDMS samples. 55

3.14 Variation of stress values with time for the PDMS/PTFE longitudinal wrinkles thin films, obtained from the stress relaxation test. 57

3.15 (a) Stress response with strain for all the samples. (b) Stress response for the PDMS sample with the PTFE film with transversal wrinkles. 58

3.16 Optical micrographs from IFM analysis of the PTFE thin film with longitudinal (a) and transversal wrinkles (b) and the PA thin film with longitudinal (c) and transversal wrinkles (c). Red bars scale: (a) 60 μm; (b) 140 μm; (c) 30 μm; (d) 30 μm. 59

3.17 Corrected absorbance assessed by PrestoBlue® viability assay with hUC-MSCs, for up to 7 days (168 hours). Results presented as Mean ± SD. 61

3.18 Scanning Electronic Microscopy (SEM) of (a) PDMS/PT membranes and (b) PDMS/PA membranes seeded with hUC-MSCs, following the sample preparation protocol including the chemical drying with HMDS. 62

3.19 Scanning Electronic Microscopy (SEM) of PDMS membranes. (a) shows PDMS membranes surface and (c, d) show PDMS membranes seeded with hUC-MSCs. EDS spectrum of the PDMS substrate. . . . 63

3.20 Scanning Electronic Microscopy (SEM) of PDMS/PT membranes. (a) shows PDMS/PT membranes surface and (c, d) show PDMS/PT membranes seeded with hUC-MSCs. EDS spectrum of the PDMS/PT substrate. 63

3.21 Scanning Electronic Microscopy (SEM) of PDMS/PA membranes. (a) shows PDMS/PA membranes surface and (c, d) show PDMS/PA membranes seeded with hUC-MSCs. EDS spectrum of the PDMS/PA substrate. 64

3.22 Scanning Electronic Microscopy (SEM) of glass coverslip seeded with hUC-MSCs. 64

3.23 Osteogenic differentiation: Alizarin Red S concentration (μM) after 21 days. Control corresponds undifferentiated control and "Diff" to osteogenic differentiation culturing conditions. Results Presented as Mean ± SD. 65

A.1 Stress variance with time for all the samples. Results obtained from the stress relaxation tests. 87

A.2 Statistical analysis of Presto Blue Viability assay of hUC-MSCs seeded scaffolds. Significance of the results is indicated according to P values with one, two, three or four of the symbols (*) corresponding to $0.01 \leq P < 0.05$; $0.001 \leq P < 0.01$; $0.0001 \leq P < 0.001$ and $P < 0.0001$, respectively; ns, not significant. 88

A.3 Statistical analysis of Quantification of Alizarin Red S concentration (μM) after 21 days. C: Undifferentiated control; D: Osteogenic Differentiation. Significance of the results is indicated according to P values with one, two, three or four of the symbols (*) corresponding to $0.01 \leq P < 0.05$; $0.001 \leq P < 0.01$; $0.0001 \leq P < 0.001$ and $P < 0.0001$, respectively; ns, not significant. 88

List of Tables

1.1 Influence of surface functional groups on protein and cellular responses (adapted from [6, 29, 30, 33]). Note: These are generalized observations and may vary depending on experimental conditions and the presence of other proteins in solution. 9

2.1 Sputtering parameters and substrates used in the preliminary studies. 21
2.2 Optimized deposition parameters for producing the final surfaces. . . 22

3.1 Amplitude and wavelength of the wrinkles on the PTFE and PA films deposited on PDMS, as well as roughness parameters determined through IFM analysis. 43
3.2 Roughness parameters of the films deposited over silicon, obtained from AFM analysis. 47
3.3 Band assignments of the absorption spectra for the PTFE target and the film resulting from its deposition [96, 97]. 49
3.4 Band assignments of the absorption spectra for the PA target and the film resulting from its deposition [98, 99]. 50
3.5 Static contact angles of the films deposited over glass and PDMS, measured with water or formamide. 51
3.6 Surface tension of the films, as a sum of dispersive and polar components. 52
3.7 Young's modulus (E), toughness (U_t) and stress (σ_r) and strain (ε_r) at rupture, determined by tensile testing. 56
3.8 Relaxation time (τ) of each tested sample and respective associated error. 57
3.9 Areas of the hysteresis loop for the 1st and 10th cycle of each sample. 59

3.10 Amplitude and wavelength of the longitudinal and transversal wrinkles on the PTFE and PA films deposited on PDMS, after the mechanical testing, as well as roughness parameters determined through IFM analysis. 60

3.11 $[Ca^{2+}]$i measured by the epifluorescence technique, using the Fura-2- AM probe in non-differentiated hUC-MSCs cells, after 10 days of cell culture in presence of the PDMS, PDMS/PT and PDMS/PA membranes, and without biomaterial, the cells were kept in culture using standard culture medium or osteogenic medium. Results are presented as mean and standard error of the mean (SD). 65

3.12 Quantification of osteogenic differentiation of hUC-MSCs seeded in PDMS, PDMS/PT and PDMS/PA membranes and cells alone, following Alizarin Red S staining protocol. Control: Undifferentiated control; Osteo Diff: Osteogenic Differentiation. Results Presented as Mean±SD. 66

Contents

List of Figures **xv**

List of Tables **xix**

Introduction **1**

1 State of the art **3**

- 1.1 Cell-biomaterial Interaction . . . 3
- 1.2 Physicochemical Surface Properties . . . 5
  - 1.2.1 Surface Chemistry . . . 6
    - 1.2.1.1 Wettability . . . 6
    - 1.2.1.2 Charge . . . 7
    - 1.2.1.3 Chemical modification techniques . . . 10
  - 1.2.2 Surface Physical and Mechanical Properties . . . 10
    - 1.2.2.1 Roughness . . . 10
    - 1.2.2.2 Surface topographic patterns . . . 11
    - 1.2.2.3 Stiffness . . . 13
    - 1.2.2.4 Fabrication of wrinkled surfaces on polymeric surfaces 14

2 Materials and Methods **19**

- 2.1 Sputtering technique . . . 19
  - 2.1.1 Materials . . . 19
  - 2.1.2 Sputtering procedure . . . 20
- 2.2 Topographic and Morphologic Characterization . . . 22
  - 2.2.1 Infinite Focus Microscopy (IFM) . . . 22
  - 2.2.2 Atomic Force Microscopy (AFM) . . . 23
  - 2.2.3 Scanning Electron Microscopy (SEM) . . . 24
- 2.3 Structural Characterization . . . 25

2.4 Chemical Characterization 26
2.5 Wettability 26
2.6 Surface Charge 29
2.7 Mechanical Characterization 30
  2.7.1 Tensile test 31
  2.7.2 Stress relaxation test 32
  2.7.3 Cyclic test 33
2.8 Tests *in vitro* 34
  2.8.1 In vitro cell viability assessment 35
  2.8.2 Ca2+ indicator Fura-2/AM loading 36
  2.8.3 Osteogenic differentiation assay 37

3 Results and Discussion 39
3.1 Preliminary Studies 39
3.2 Topographic and Morphologic Characterization 41
3.3 Structural Characterization 47
3.4 Chemical Characterization 48
3.5 Wettability 51
3.6 Surface Energy 52
3.7 Zeta Potential 53
3.8 Mechanical Properties 53
  3.8.1 Tensile Test 54
  3.8.2 Relaxation Stress Test 56
  3.8.3 Cyclic Tests 57
  3.8.4 Surface characterization after mechanical testing 59
3.9 *In vitro* Tests 60
  3.9.1 Cell Viability 60
  3.9.2 Intracellular calcium 64
  3.9.3 Osteogenic Differentiation: qualitative and semi-quantitative analysis 65
  3.9.4 Discussion - *In vitro* tests 66

Conclusions 69

Bibliography 73

Appendices **85**
A Appendix 87

Nomenclature

Acronyms

AFM	Atomic Force Microscopy
ARS	Alizarin Red S
ATR	Attenuated Total Reflectance
DC	Direct Current
ECM	Extracellular Matrix
FBS	Fetal Bovine Serum
FTIR	Fourier Transform Infrared Microscopy
HMDS	Hexamethyldisilazane
hUC-MSCs	Human Umbilical Cord Mesenchymal Stem Cells
IFM	Infinite Focus Microscopy
MSCs	Mesenchymal Stem Cells
PA	Polyamide
PBS	Phosphate Buffer Solution
PDMS	Poly(dimethylsiloxane)
PTFE	Poly(tetrafluoroethylene)
PVC	Polyvinyl Chloride
RF	Radio Frequency
RGD	Arginyl-Glycyl-Aspartic
SAM	Self-assembled Monolayer
SD	Standard error of the mean
SEM	Scanning Electron Microscopy
SPM	Scanning Probe Microscopy
XDR	X-ray Diffraction

Symbols

$\boldsymbol{\lambda}$	Wavelength
$\mathbf{A}$	Amplitude
$\mathbf{d}$	Interplanar spacing
$\mathbf{n}$	Diffraction order
$\boldsymbol{\theta}$	X-ray scattering angle
$\boldsymbol{\gamma_{LV}}$	Surface tension at the liquid-vapor interface
$\boldsymbol{\gamma_{SL}}$	Surface tension at the solid-liquid interface
$\boldsymbol{\gamma_{SV}}$	Surface tension at the solid-vapor interface
$\boldsymbol{\theta}$	Static contact angle
$\boldsymbol{\theta_a}$	Advancing stable angle
$\boldsymbol{\theta_r}$	Receding stable angle
$\boldsymbol{\theta^*}$	Angle on the roughness-free surface
$\mathbf{r}$	Roughness factor
$\mathbf{f}$	Fraction of the surface in contact with the liquid
$\boldsymbol{\gamma_s}$	Surface tension of the film
$\boldsymbol{\gamma_S^d}$	Dispersive component of the film surface tension
$\boldsymbol{\gamma_S^p}$	Polar component of the film surface tension
$\boldsymbol{\gamma_L}$	Surface tension of the liquid
$\boldsymbol{\gamma_L^d}$	Dispersive component of the liquid surface tension
$\boldsymbol{\gamma_L^p}$	Polar component of the liquid surface tension
$\boldsymbol{\zeta}$	Zeta potential
$\mathbf{E}$	Young's Modulus
$\boldsymbol{\sigma}$	Stress
ε	Strain
$\boldsymbol{\eta}$	Viscosity of the fluid
$\boldsymbol{\tau}$	Relaxation time
$\boldsymbol{\sigma_0}$	Initial stress
$\mathbf{t}$	Time
$\boldsymbol{A_0}$	Specimen initial cross-sectional area
$\boldsymbol{l_0}$	Specimen initial length
$\boldsymbol{l_i}$	Specimen length
$\boldsymbol{F}$	Force
$\boldsymbol{U_t}$	Toughness
$\boldsymbol{\sigma_r}$	Stress at rupture
$\varepsilon_{\boldsymbol{r}}$	Strain at rupture
$\boldsymbol{U_t}$	Toughness

Introduction

In order to understand how to make the best substrate for cells *in vitro* we have to understand how they interact with their environment *in vivo*.

Over the past decades, it has been demonstrated that cells can sense and respond to their surroundings [1–3]. The extracellular matrix (ECM), which is a part of their environment, is a highly complex fibrous mesh composed of proteins (e.g. collagen, laminin, fibronectin, elastin), glycosaminoglycans (e.g. hyaluronic acid, heparin), proteoglycans and growth factors. This matrix not only plays an important role in providing support to tissues but also directs a diverse set of functions in individual cells [4]. Both chemical (energy, polarity, wettability, zeta potential) and physical properties (stiffness, topography, and ligand presentation) of the extracellular matrix have been shown to affect cell behavior [5–7]. Cell adhesion to the ECM, mainly via integrins, stimulates signaling pathways that regulate survival, proliferation, migration and differentiation [8].

In the context of biomaterials, the perfect surface should mimic the ECM. Thus, the importance of both physical and chemical properties of a biomaterial becomes clear. The ability of optimize these properties to promote a good cell-material interaction will increase the biocompatibility and the probability of success of the biomaterial.

When designing a substrate, a scaffold or a biomaterial, it is possible to introduce chemical modifications, for instance by grafting of chemical groups, adhesion ligands and growth factors [9]. But, not only the chemistry of the surface can be modified, also the physical properties can suffer alterations [10]. It is in this context that this project arises, with a main purpose of modifying the topography of certain materials through the formation of wrinkling patterns on its surfaces, at a nano- and micrometer scale. Microtopographies are able to guide the shape and motility of the cell body by physical confinement or alignment and typically result in whole-cell contact guidance [11]. In contrast, nanotopographies are several orders of magnitude smaller than the cell body, but have a similar size to sub-cellular structures, such as F-actin, filopodia and integrin receptors [1, 12].

Most tissue extracellular matrices, such as bone, tendon, nerve and myocardium, have regular architectures consisting of well-aligned micro- and nano-scaled fibrous structures [13]. Increasing evidence suggests that an aligned topographical structure is essential for cell alignment and tissue morphogenesis as well as remodeling to allow the effective and accurate expression of tissue function [14].

Several studies with wrinkling topographies have been getting promising results, as they appear to influence several cell functions, such as cell adhesion and alignment [15–18].

In the present work, thin films of poly(tetrafluoroethylene) (PTFE) and polyamide (PA) were deposited on poly(dimethylsiloxane) (PDMS) substrates using the sputtering method, obtaining different wrinkling topographic patterns as a function of the substrate's thickness and the existence/absence of a mechanical tension. Ordered wrinkle patterns in a specific direction were obtained by stretching the polymer prior to the deposition. Besides the topography, the use of two distinct materials for the substrate modification allowed to assess the influence of the chemistry in cell behavior.

The work developed in this project is expected to contribute to several potential applications in the fields of tissue engineering and soft electronics, for example robot hands where fingers require roughness for sensing to be possible. When a biomaterial is developed with the intent of being inserted in the body, its mechanical properties are of great importance because they should mimic or at least be as similar as possible to the properties of the biological material present on the environment where they are supposed to be implanted. Mechanical tests were then performed on the samples obtained in order to characterize them and study how their topography was affected by the application of tension.

The samples developed were also tested for *in vitro* cell viability and evaluated in their capacity to promote and or inhibit osteogenic differentiation in Human Umbilical Cord Mesenchymal stem cells (hUC-MSCs).

This dissertation is composed of three chapters. The first one consists of a brief bibliographical review where the most relevant matters for this project are discussed, such as the cell-biomaterial interactions and the physical and chemical properties of the surface. The second chapter is dedicated to the methodology used throughout the project development. The third and last chapter concerns the results obtained and its discussion.

1

State of the art

1.1 Cell-biomaterial Interaction

An appropriate cellular response to implanted surfaces is essential for the success of the chirurgical procedure as well as for tissue regeneration and integration. When a biomaterial is put into contact with a living system, several physicochemical interactions occur at the interface. These interactions have a high degree of specificity, requiring initial recognition, physical adhesion, electrical and chemical communication, cytoskeletal reorganization, and/or cell migration.

Biological materials have certain motifs which make them recognizable by the immune system. However, this is not the case with engineered materials. In fact, several biological responses often take place after implantation, such as blood clotting and foreign body reaction, which indicates that the body recognizes these non-biological materials as invaders [19]. The triggering step of this reaction is the adsorption of proteins on the surface of the biomaterial, that are recognized by the integrin receptors present on most cells. The adsorbed proteins, rather than the surface itself, are the responsible for the initial response of the cells. In fact, as stated by Boyan et al., “cells do not see a naked material, *in vivo* or in culture (. . .) the material is conditioned by the components of the fluid in which the material is immersed” [20]. Once a biomaterial is implanted, it is immediately coated with proteins from blood and interstitial fluids, and it is through this adsorbed layer that cells can sense foreign surfaces and also interpreter their structure and composition [21]. More precisely, cells depend on specific proteins for anchorage and extracellular instructions, which is why the composition of this adsorbed layer is a key mediator of cell behavior. Among these proteins we can find fibronectin, vitronectin, collagen, laminin, which are ECM adhesion proteins [22].

After the adsorption of proteins, cells arrive at the implant surface, where they can differentiate, multiply, communicate with other cell types and organize themselves into tissues. Cells secrete ECM molecules that fill the spaces between

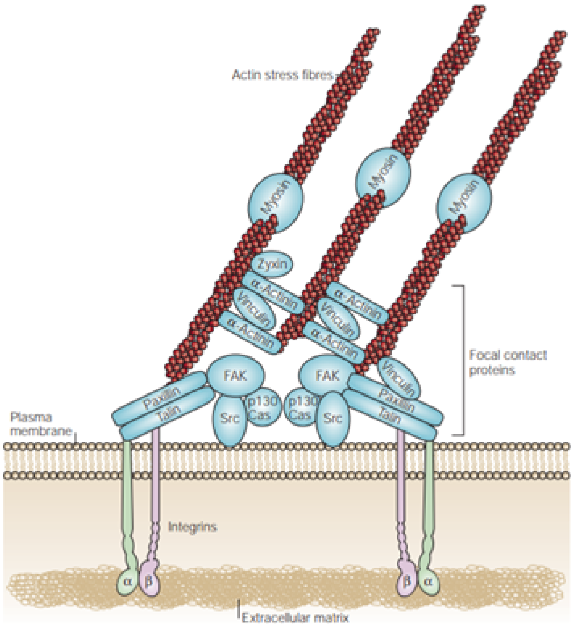
Actin stress fibres
Myosin
Myosin
Myosin
Zyxin
α-Actinin
Vinculin
α-Actinin
α-Actinin
Vinculin
α-Actinin
Vinculin
Focal contact proteins
FAK
FAK
Paxillin
Talin
p130 Cas
p130 Cas
Src
Src
Paxillin
Talin
Plasma membrane
Integrins
α
β
β
α
Extracellular matrix

Figure 1.1: Molecular architecture of focal contacts [25].

them and serve as attachment structures [19]. In fact, cells adhere to surfaces through specific binding sites located on the adhesion proteins, such as the Arginyl-Glycyl-Aspartic acid (RGD) motif (found in proteins such as fibronectin, laminin, or vitronectin), or the L-α-Aspartylglycyl-L-α-glutamyl-L-alanine (DGEA) and Glycine-Fhenylalanine-Hydroxyproline-Glycine-Glutamate-Arginine (GFOGER) motifs (found in collagen). This connection is mediated by specific cell receptors, mostly integrins.

Integrins are heterodimeric transmembrane proteins, formed by an alpha and beta subunit, which are fundamental to mechanically link the extracellular substrate to the cytoskeleton (more precisely actin filaments). The integrins exhibit low affinity and high abundance, so that they can bind weakly to several different but related matrix molecules [23]. Within the cell, the intracellular domain of integrin binds to the cytoskeleton via adapter proteins such as talin, α-actinin, filamin, vinculin and tensin. Many other intracellular signaling proteins, such as focal adhesion kinase (FAK), bind to and associate with this complex. The clustering of several complexes like these, forms the basis of a focal adhesion (Figure 1.1) [24].

Focal adhesions are responsible not only for anchoring cells to the ECM, but also for signal transduction, which inform the cells about the condition of the ECM, and vice versa, thus affecting their behavior. Focal adhesions can be constantly assembled and disassembled, for example, for a cell to be able to migrate, its cytoskeleton must be rearranged and the cell has to establish new contacts in the direction of movement and break old focal contacts at the opposite edge.

Both chemical (energy, polarity, wettability, zeta potential) and physical properties (stiffness, topography, and ligand presentation) of the extracellular matrix have been shown to affect cell behavior [5,23,24].

Many surface properties, such as chemistry and topography, can be manipulated in an effort to selectively control the cell–material interaction. On the basis of this information there has been much research in this area, including studies focusing on the structure and composition of the implant interface, optimization of biological and chemical coatings and elucidation of the mechanisms involved in the subsequent cell–material interactions, in order to optimize it and to increase the biocompatibility and probability of success of the biomaterial [6,7].

The next section will be dedicated to the influence of the chemical and physical properties of a biomaterial on cell behavior.

1.2 Physicochemical Surface Properties

The relationship established between cells and biomaterials, briefly discussed in the previous section, is very complex and has many questions still left unanswered. However, it is known that concepts such as protein adsorption, cell adhesion and signal mechanotransduction, are substrate-dependent. The immediate reaction following implantation is the result of interaction between biomolecules and surface where properties/characteristics such as hydrophobicity, charge, chemistry and topography all influence the biological response. Proteins adsorb in differing quantities, densities, conformations, and orientations, depending on these chemical and physical properties of the surface, which in consequence dictates cell behavior [9,10,26]. Two paths can be followed to modify a surface: i) altering the atoms, compounds, or molecules of the surface (chemical modification, etching, mechanically roughening); or ii) coating the surface with a material with similar or dissimilar chemical composition (coating, grafting, thin film deposition) (Figure 1.2).

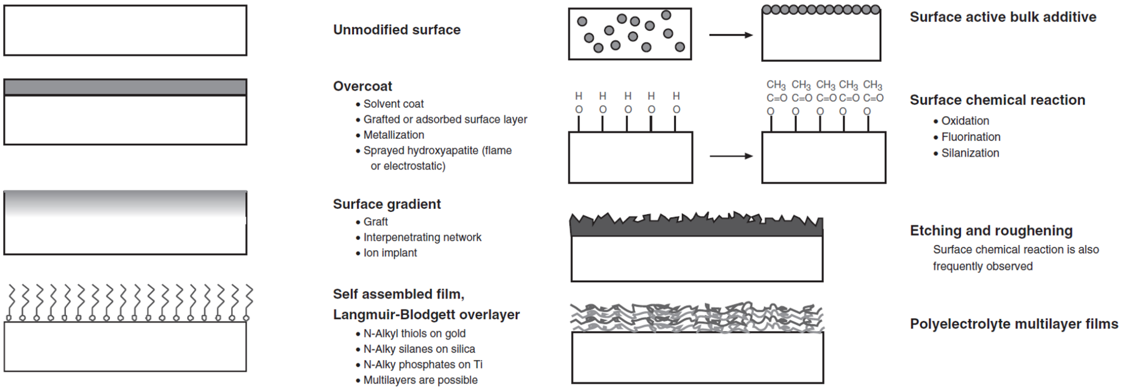
Unmodified surface
Overcoat
• Solvent coat
• Grafted or adsorbed surface layer
• Metallization
• Sprayed hydroxyapatite (flame or electrostatic)
Surface gradient
• Graft
• Interpenetrating network
• Ion implant
Self assembled film, Langmuir-Blodgett overlayer
• N-Alkyl thiols on gold
• N-Alky silanes on silica
• N-Alky phosphates on Ti
• Multilayers are possible
H H H H H
O O O O O
CH_3 CH_3 CH_3 CH_3 CH_3
C=O C=O C=O C=O C=O
O O O O O
Surface active bulk additive
Surface chemical reaction
• Oxidation
• Fluorination
• Silanization
Etching and roughening
Surface chemical reaction is also frequently observed
Polyelectrolyte multilayer films

Figure 1.2: Surface modification methods. Adapted from [19].

1.2.1 Surface Chemistry

The chemical composition of a biomaterial surface, which defines its energy, polarity, wettability and zeta potential, dictates the adsorption and conformation of the protein layer that readily covers the surface as soon as the implantation takes place and serves as substrate for integrin mediated cell adhesion, affecting the character of the cell-material interaction. Protein adsorption is a complex process involving van der Waals, hydrophobic and electrostatic interactions, and hydrogen bonding. Although surface-protein interactions are not well understood, surface chemistry has been shown to play a fundamental role in protein adsorption [26].

1.2.1.1 Wettability

The wettability of a surface, as well as its energy, can be determined by the contact angle measured between the material surface and a liquid of a certain polarity. A low contact angle between the material and water indicates good spreading of water on the surface, i.e. hydrophilicity of the material, while a high contact angle is a characteristic of hydrophobic surfaces. The hydrophilicity or hydrophobicity of a surface can be further characterized by its zeta potential [6]. According to Vogler, evidence from more than a decade of intermolecular force research on biomaterials interaction suggests that hydrophobic surfaces exhibit water contact angles greater than 65°, whereas hydrophilic surfaces exhibit water contact angles below 65° [27].

Water is a polar solvent, with a high surface tension (γ_L=72 mJ/m^2) which means that it does not readily interact with nonpolar solutes and surfaces. Proteins present a folded structure, with their hydrophobic residues positioned away from the water due to interactions of the acidic, basic, polar and nonpolar aminoacid side chains with water and with each other. However, about 40-50% of protein surface is composed of nonpolar groups, making proteins more likely to adsorb on hydrophobic surfaces. Thus, hydrophilic surfaces form tighter bonds with water, which makes it harder for proteins to adsorb. Therefore, if proteins are more likely to adsorb on hydrophobic surfaces, cells will also adhere more. However, to overcome the energy barrier associated with surface adsorption, proteins can suffer conformational changes that may affect its activity by either exposing or hiding different functionalities, such as the RGB recognition sequence or the receptor site for inflammatory cells [21,27–29]. In contrast, on hydrophilic surfaces, there is a competition between water molecules and proteins since water forms hydrogen bonds with the surface. This results in less protein adsorption and less conformational change, which makes the adhesion site accessible to the receptors, that then cluster into focal adhesion plaques and communicate with other focal adhesion proteins and the actin cytoskeleton (Figure 1.3) [22, 26, 30].

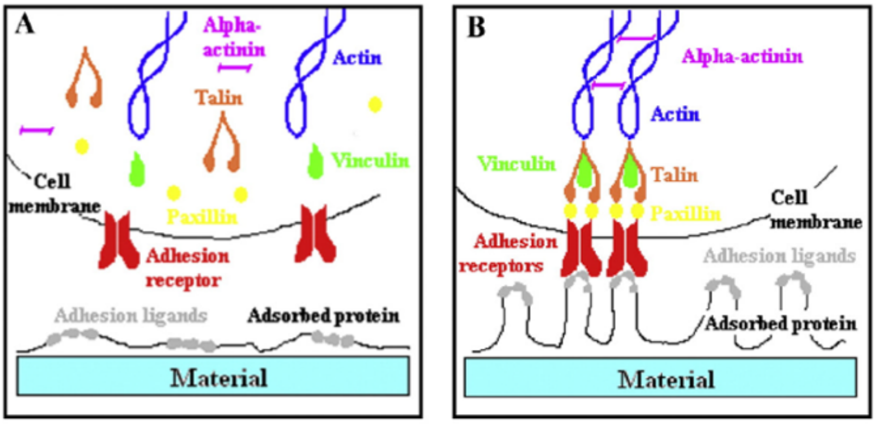
A
Alpha-actinin
Actin
Talin
Vinculin
Cell membrane
Paxillin
Adhesion receptor
Adhesion ligands
Adsorbed protein
Material
B
Alpha-actinin
Actin
Vinculin
Talin
Cell membrane
Paxillin
Adhesion receptors
Adhesion ligands
Adsorbed protein
Material

Figure 1.3: Scheme of the adsorption of an adhesion protein to (A) a hydrophobic material surface and (B) a hydrophilic surface [6].

Usually, polymers used for tissue engineering are mostly hydrophobic, which implies that they have a high affinity to a great number of proteins. Surface modifications arise in an attempt to accurately control the cellular response, without interference of nonspecific cell or protein interaction, by chemical modifications and by grafting of cell adhesion ligands or chemical groups.

A controlled adhesion environment is difficult to achieve when relying upon protein adsorption to facilitate cell adhesion. This process is unstable, as proteins can desorb or change conformation. These limitations have prompted the use of adhesive proteins and small peptide segments covalently immobilized upon biomaterials in order to control cell adhesion [31]. The covalent attachment of short peptide sequences to substrates is thought to be the best solution, as it is sufficient to promote cell adhesion and has the benefits of being less susceptible to denaturation and proteolysis [9, 32].

1.2.1.2 Charge

Surface functional chemical groups determine the charge of a material surface and its behavior when in contact with an aqueous environment. The surface charge significantly contributes to processes such as protein adsorption or biofilm formation. For the analysis of surface charge, the zeta potential at the material-water interface is commonly employed.

It is common sense that opposite charges attract each other. This fact is important when considering the biological responses to implanted materials, as cell membranes have a negative charge which, in theory, means that they prefer to adhere on positive charged surfaces. However, although interactions between negatively charged cell membranes and charged substrate are significant, Davies and colleagues point out that these alone are not sufficient to explain the observed differences in adhesion and migration of cells on both positively and negatively charged surfaces [21].

An approach to better understand and control cell-material interactions is grafting chemical groups onto a material surface to provide charged molecules, enabling additional protein binding [9]. The use of functional groups such as $-CH_3$, $-OH$, $-COOH$ and $-NH_2$ has been widely studied with this purpose (Table 1.1).

Table 1.1: Influence of surface functional groups on protein and cellular responses (adapted from [6, 29, 30, 33]). Note: These are generalized observations and may vary depending on experimental conditions and the presence of other proteins in solution.

Methyl ($-CH_3$)	Neutral, hydrophobic	Abundant adsorption of fibrinogen; high protein adsorption, usually in conformations unfavorable for desired cellular interactions; increased leukocyte adhesion.
Hydroxyl ($-OH$)	Neutral, hydrophilic	Low protein affinity; tight binding to fibrinogen; increase in oxygen containing functionalities proportional to cell growth; increases cell adhesion strength; high levels of osteoblasts differentiation and mineralization.
Amine ($-NH_2$)	Positive, hydrophilic	Forms hydrogen bonds with fibrinogen; promotes exposure of focal adhesion components by adsorbed fibronectin; increased endothelial cell and fibroblasts growth and osteoblasts differentiation and mineralization; enhances myoblast proliferation.
Carboxyl ($-COOH$)	Negative, hydrophilic	Preferential interaction with fibronectin and albumin; cell growth dependent on –COOH concentration; low levels of osteoblast and myoblast differentiation but high cell proliferation levels.

In recent years, research has progressed to the evaluation of mixed functional group chemistries on surfaces. The goal of these studies is to attempt to combine favorable properties of both functionalities onto one surface to enhance biocompatibility. For example, concerning surface adhesion, it was observed that hydrophobic self-assembled monolayers (SAMs) combining $-COOH$ and $-CH_3$ groups induce higher cell adhesion than hydrophilic $-COOH$ and $-OH$ SAMs [29].

1.2.1.3 Chemical modification techniques

Although chemical modifications have been showing promising *in vitro* results, low success has been achieved in vivo due to the lack of well-defined surfaces (only differ in 1 or 2 properties) and well-characterized animal implantation models.

Some modification techniques for creating homogeneous and well-defined surfaces are:

- Chemical graft modification: Immobilization of compounds onto the surface, usually involving a covalent conjugation of either a protein or monomer to alter its chemistry; long-term stability; loss of protein mobility and conformational change.
- SAM techniques: Method to more precisely control the density and conformation of a single or multiple specific functional group or a surface; limited to gold coated or silver coated surfaces.
- Plasma techniques: obtained when gases are excited into energetic states by radio frequency, microwave, or electrons from a hot filament discharge; uniformly modifies surfaces regardless of geometry, allowing modification of nano- and microparticles and films, for use in tissue engineering and artificial organs; economic, effective, environmentally green and with a high level of film chemistry controllability [29].

-

1.2.2 Surface Physical and Mechanical Properties

When studying cell behavior in the presence of a biomaterial it is a fact that chemistry has a significant role in the outcome. However, a path that initially seemed not that obvious revealed itself as one of the principal factors affecting biomaterial success: its topography. Through a process known as mechanotransduction, various physical cues in the cells surrounding environment are integrated and converted to biochemical responses that lead to changes in cell function [34]. These changes are responsible for affecting cell shape and orientation, as well as cell adhesion and differentiation.

1.2.2.1 Roughness

The roughness of a surface is a concept worth discussing, as it is thought to be highly correlated with cell adhesion. Considering that the ECM is composed of several nano- and micro-rough structures, mimicking this environment makes sense in an attempt of studying its influence on cell behavior. The macro roughness, with irregularities higher than 100 μm, usually does not restrict cell adhesion and spreading and may enhance the anchorage of the implant in the surrounding bone tissue. However, the majority of cells have a size several orders of magnitude lower, which does not allow them to recognize the irregularities and percieve the surface as smooth [6, 35]. Considering the submicro- and microscale, with irregularities comprised between 0.1 μm and 100 μm, and the nanoscale, with features below 100 nm, a lot of research has been developed, with a wide range of results depending upon many factors, including cell type, feature size, geometry, and the physical-chemical properties of the substrate [12]. Additionally, as previously described, cell adhesion is related to protein adsorption, which will be influenced by the surface morphology considered at the nanometer scale [22]. Thus, for a better understanding of relevant topographic features, it is important to vary one specific parameter at a time, in order to determine its impact on cellular functions [36]. Overall, the studies appear to agree that at the nanometer length scale, the topography affects sub-cellular behaviors (1-10 μm) such as the organization and clustering of integrins [35, 37, 38], whereas at the micrometer level, cellular and supracellular characteristics (100-1000 μm) such as cell shape and motility, and tissue organization are influenced [33, 34]. Moreover, some studies indicate that the combination of nano- and microscale topography could induce better results then those achieved by using each single sizescale [38].

Topographical features of different length scales ranging from nano- to micrometer have strong influences on cell adhesion, morphology, alignment, and contact guidance. In addition, there might exist an optimal size range in which these cell behaviors are most significantly improved, although depending on cell type, substrate material, and structure of topography. For example, when 3T3 fibroblasts and MG63 osteoblast cells were grown on nanoparticles of increasing diameters (16, 38 and 68 nm) a critical nanoparticle density (50–140 particles/μm^{-2}) was identified to encourage cell adhesion on 16 nm diameter substrates, whereas on 68 nm diameter substrates, the attachment decreased for both cell types [38, 39]. Also, if the irregularities are rounded and relatively distant, they might be beneficial or neutral for cell spreading and growth, while for sharp and densely distributed features these properties may be attenuated [35].

1.2.2.2 Surface topographic patterns

Up to now, a wide variety of surface topographic patterns were fabricated and mentioned in the literature concerning cell function, such as grooves, pits, posts or pillars, wrinkles and fibrous (Figure 1.4). For the fabrication of these patterned surfaces, several techniques have been developed. One of the most popular method for micropatterning is photolithography; several techniques of soft lithography, such as microcontact printing, and transfer lithography have also been used for patterning at this scale. When considering nanopatterning techniques, the most appropriate for cell studies are e-beam lithography or etching, dip-pen nanolithography and block copolymer micelle nanolithography [34, 40].

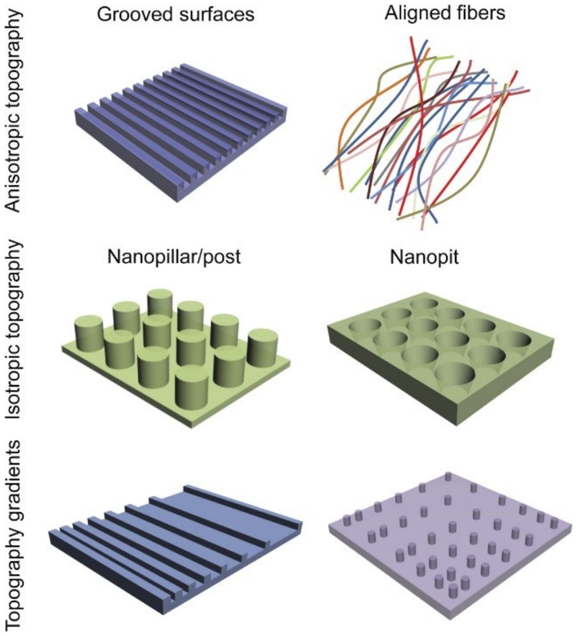

Figure 1.4: Schematics of surface topographic patterns commonly used as cell culture substrates [7]

A famous phenomenon occurring when studying topographic features is contact guidance: cell alignment on an anisotropic surface. Usually, the contact guidance leads cells to elongate along groove or ridge axes, where most of cells presented a round shape on smooth substrates [18, 41, 42]. However, not all types of cells prefer aligning along the groove axes. In fact, Webb et al. observed that hippocampal and cerebellar granule neurons extended their neurites perpendicular to the grooves [40, 43]. Contact guidance has been considered an essential component regulating cell migration, which can be directed by both the local density and anisotropy of the topography features [40]. Usually, enhanced migration is observed when cells present elongated morphology and alignment with the nanograting axis [12, 44]. Also, grooves have been extensively investigated. Culturing cells on substrates with these features usually results in significant alterations in cell morphology and cytoskeletal arrangement, as the cells align along the long axis of the groove, with cytoskeletal elements such as actin and microtubules also organizing themselves parallel to grooves 1 [32, 45]. For example, endothelial cells on a PDMS grooved substrate (3.5 μm width 0.2-5 μm depth) showed increased alignment of cells with increasing groove depth and alignment of F-actin and vinculin along the grooves [46]. Another advantage of this type of feature is the possibility of systematically modify its width [36].

Substrates with nanopost and nanopit features elicit a more subtle effect on cellular morphology [12]. Several studies have shown that pit topographies can produce different effects on cellular adhesion and alignment in vitro, depending on pit size, spacing and symmetry [47]. Kidambi et al. observed that 3T3 fibroblasts, HeLa cells, and primary hepatocytes prefer to adhere on smooth surfaces compared to micrometer pit topography surfaces and the number of attached cells decreased with pit diameter [48].

Most tissues extracellular matrices have regular and anisotropic architectures consisting of well-aligned micro-/nano-scaled fibrous structures. Increasing evidence suggests that an aligned topographical structure is essential for cell alignment and tissue morphogenesis [49, 50]. In an attempt of mimicking the native cell microenvironment, surface wrinkling appears as a rapid and inexpensive approach for fabricating topographically patterned surfaces with multiscale topographical cues [31] (Figure 1.5). As the control over both the wavelength and amplitude of a wrinkled surface has increased, several studies were made on their impact on surface properties [15, 17]. Moreover, different cell types cultured on wrinkled substrates showed to align along the wrinkles direction [51].

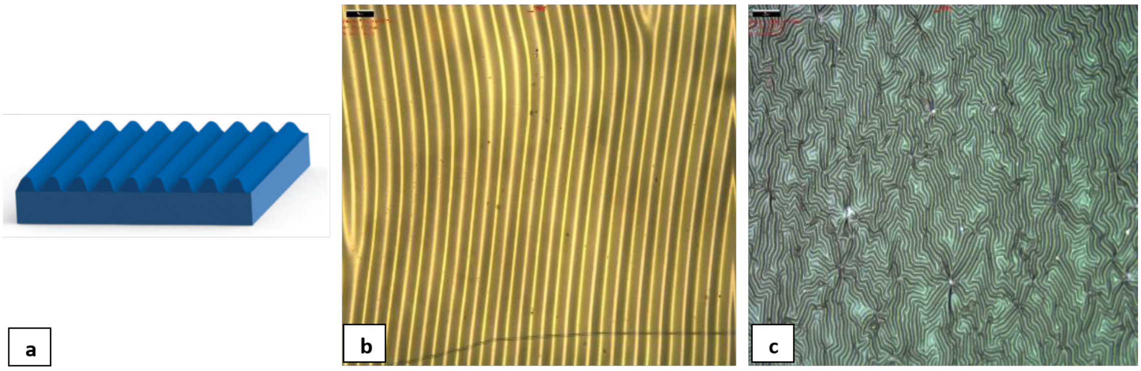

Figure 1.5: (a) Scheme of a wrinkled surface pattern. (b and c) Optical micrographs of PDMS substrates of different thicknesses after PTFE thin film deposition, resulting in aligned distribution in (b) and random displacement in (c) (current work).

1.2.2.3 Stiffness

The human body is composed of many tissues with different mechanical properties able to control physiological processes. One example is the embryonic development, which is dependent on mechanical forces [9]. The stiffness of a surface is a property that has been considered important in the formation of cell–substrate adhesion complexes, cell spreading, survival, growth and cell fate [6]. When the surface is too soft (modulus of elasticity (E) of 1 kPa) cells are not able to adhere and spread, which ends in cell apoptosis, even if the surfaces have been functionalized with cell adhesion proteins. The material must be able to resist the tractional forces generated during cell adhesion and spreading [52]. Considering cell differentiation, Engler *et al.* have demonstrated that on very soft polyacrylamide gels (E=0.1–1 kPa), mimicking the mechanical properties of soft brain tissue, human mesenchymal stem cells (MSCs) differentiated towards the neuronal phenotype. However, on harder gels (E=8 to 17 kPa), mimicking muscle tissue, MSCs acquired a myogenic phenotype. Also, on the stiffest matrices (E=25 to 40 kPa) MCSs become osteogenic [6, 35, 53]. Besides differentiation, the mechanical properties of a substrate are also able to control self-renewal of stem cells. Stem cells from skeletal muscle revealed increased proliferation with rising stiffness of the material [9]. It is also worthy to mention that not only stiffness is responsible for stem cells fate. It has been suggested that specific surface patterns can either maintain MSCs in an undifferentiated state [54] or boost their differentiation towards specific cell types [55]. Also, the surface roughness, whether it is on the micro- or nanometer scale, has shown to have an influence on this matter [56]. It is essential to better understand which precise specifications of surface patterns can direct differentiation towards one lineage or another [36].

The key to control the biological responses of cells is the combination of both chemical and topographic alterations in a very personalized manner for each intended application. However, when a physical modification of a surface occurs it is usually correlated with a chemical modification, which makes it difficult to separate the influence of both chemical and physical properties on the event of study.

1.2.2.4 Fabrication of wrinkled surfaces on polymeric surfaces

Wrinkles can be formed on polymeric surfaces through several strategies that usually use films:

(1) Films formed by a system with multiple (two or more) layers, including the substrate (Figure 1.6); (2) Homogeneous films; (3) Films formed by a gradual variation of the mechanical properties from the surface to the bulk.

In this dissertation, the approach used falls into the 1st category, as the formation of wrinkles occurs in a system of multiple layers. This way, the other types of films will not be further discussed here (however there's a review on their formation made by Rodríguez-Hernández [57]).

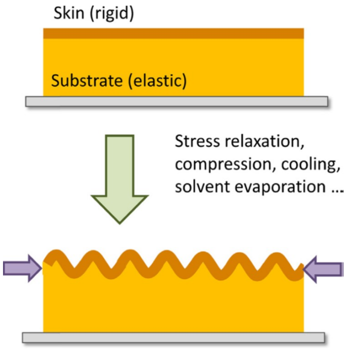
Skin (rigid)
Substrate (elastic)
Stress relaxation, compression, cooling, solvent evaporation ...

Figure 1.6: Schematic representation of wrinkle formation in a structure composed of two layers [57].

Layered films are composed of two or more layers with distinct mechanical properties, namely different Young's modulus and coefficients of thermal expansion. A rigid top layer over an elastic one can be obtained by exposing the elastic layer to a physical treatment, altering the mechanical properties of its surface, or coating the elastic substrate with a stiffer film. Wrinkles are formed by relaxing the stress applied on the elastic layer, which may be applied before or after the appropriate surface treatment. For example, wrinkles can be obtained either upon removal of mechanical tension or by applying a mechanical compression in bilayer films. Moreover, stimulus such as thermal variations or swelling can also induce wrinkles [57,58]. Expansion occurs during heating of an elastic substrate. When a physical surface treatment occurs, or a stiffer coating is deposited onto it, followed by subsequent cooling of the polymer, the stiff layer suffers compressive stress, ending up wrinkling.

A study conducted by Ferreira [28], concluded that the sputtering technique enables the formation of wrinkled surfaces as a result of temperature variation and differences between the coefficients of thermal expansion of the film and the substrate. Also, the wrinkling of thin sheets, when a mechanical tension is applied, depends on the direction of the applied force [58]. Ozhono and Shimomura observed that applying a small uniaxial stress to platinum sputtered PDMS samples, caused the wrinkles to align perpendicularly to the direction of the stress and only 7% strain was needed to achieve almost perfect wrinkle alignment [59]. As said previously, evidence suggests that an aligned topographical structure is essential for cell alignment and tissue morphogenesis [49, 50]. Within this frame, this work intends to create aligned wrinkling surfaces through sputtering of polymers (PTFE and PA) onto PDMS substrates previously strained.

Magnetron sputtering

The sputtering method occurs in a vacuum chamber, where a potential difference is applied between a target (cathode) and a substrate (anode), causing a luminous electric discharge between them (Figure 1.7). The plasma is created by ionization of a sputtering gas, generally a chemically inert gas like Argon. The electrons collide with the gas atoms ionizing them and producing more electrons that continue the process. The target, subjected to a negative potential, attracts the positive ions that after collision produce, by momentum transfer, the ejection of atoms (or atoms aggregates) from the target. The ejected species go through the plasma and arrive as adatoms onto the substrate. Depending on the energy, the adatoms diffuse and bound on specific sites of the substrate, usually low energy locations. This process continues as the coating is build-up [60].

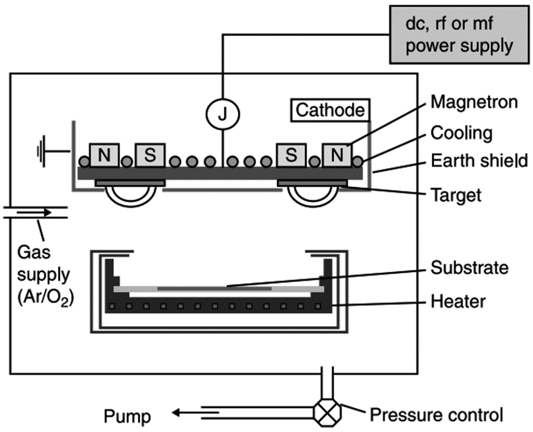

Figure 1.7: Scheme of a magnetron sputter device. Adapted from [61].

Conductive materials can be deposited using a direct current (DC) power supply. However, if the target is an insulator, e.g. a polymer, it accumulates positive charges that leads to the extinction of the plasma. This problem can be overcome using a radio frequency (RF) power supply, which will create a continuous negative potential on the target.

The introduction of a magnetic field with magnetrons will induce the electrons to describe helical orbits. This will increases the negative charge near the target which, in turns, attracts more positive ions thus resulting in a significant increase of the deposition rate.

The wrinkling pattern on the surface, created during sputtering, is due to temperature variations and the difference between the thermal expansion coefficients of the substrate and the coating [28]. There is very little information available in the literature about sputtering polymers onto polymers in order to promote the creation of wrinkled surfaces. In this work, the sputtering technique is used to deposit thin films of PTFE and PA onto PDMS substrates.

2

Materials and Methods

2.1 Sputtering technique

2.1.1 Materials

The material chosen as substrate was polydimethylsiloxane (PDMS), provided by ISR-UC, which is a popular elastomer used in micro- and nanofabrication. It is biocompatible and highly permeable to gases; it also has good thermal and chemical stability. It's hydrophobic and has a low elasticity modulus (1.8 MPa), making it susceptible to external stimuli deformations, and, subsequently favorable to wrinkles formation [62].

To evaluate the properties of the film without wrinkles, other sputtering substrates were used: glass, silicon and stainless steel (316L, AISI-American Institute Steel and Iron), allowing to obtain distinct topographies with the same chemical composition.

In order to consider distinct chemical compositions and to study their influence in cellular behavior, two different polymers were chosen as targets for the sputtering method: polytetrafluoroethylene (PTFE) and polyamide 6.6 (PA). The targets with 99.5% purity, 100 mm diameter and 5 mm thickness, were purchased from Goodfellow (UK), The discharge gas used was Argon (Ar) with 99.9999% purity (from Air Liquide S.A.).

PTFE presents a high degree of crystallinity, in the range of 89-98% [63], is hydrophobic and has a Young's modulus of about 0.3-0.8 GPa. It is considered the engineering polymer due to its chemical stability and its high melting temperature, around 342 °C [64].

Polyamide 6.6 (PA), or Nylon®, is also a semi-crystalline polymer made of repeating units linked by amide bonds. It possesses high strength and stiffness. It is resistant to aging at high temperatures and has outstanding chemical resistance, although not as high as the one presented by PTFE [65].

Before entering the sputtering chamber, the PDMS substrates were submitted to a cleaning process in ultrasounds. The substrates were sequentially immersed in acetone, alcohol and deionized water, 10 minutes in each liquid and then dried in a hot air current. After this process, the substrates were placed on the substrate holder with spring clips: (i) directly on the substrate holder; (ii) on a grid over the substrate holder; (iii) on the grid with a defined applied strain.

In the case of the glass, silicon and stainless steel, the fixation was made directly on the substrate holder with conductive glue.

2.1.2 Sputtering procedure

The equipment used for the sputtering technique was Edwards Coating System E306A, which operates in 13.56 MHz radiofrequency mode and is composed of three power sources: two connect to two cathodes and one connected to the substrates, thus enabling the simultaneous deposition from two targets.

Before the deposition, a plasma cleaning was performed to clean the target and the substrate. A shutter is positioned between the substrate holder and the target which avoids cross-contamination.

In a first phase of this project, tests were performed on PDMS substrates with different thicknesses, subjected or not to a mechanical strain. Details on the sputtering conditions used are presented in the Table 1.

Table 2.1: Sputtering parameters and substrates used in the preliminary studies.

Assay	**Substrate thickness(μm)**	**Strain (%)**	**Substrate**	**Target**	**Parameters**	
					Cleaning	**Deposition**
AJ_1 (on the grid)	200 400 1000 2000	0	PDMS	PTFE	Pressure= 0.7 Pa Power= 100 W D= 0.002546 W/mm^3 t=5 min	Pressure= 1.3 Pa Power= 150 W D= 0.00382 W/mm^3 t=15 min
AJ_2 (on the substrate holder)	200 400 1000 2000	0				
AJ_3 (on the substrate holder)	200 400 1000	10				
AJ_4 (on the substrate holder)	200 400 1000	30				
AJ_5 (on the substrate holder)	200 400 1000	15				

On a second phase of tests, PTFE and PA were sputtered onto PDMS substrates pre-strained with 10% tension. In addition, sputtering of PTFE and PA were performed with glass, silicon and stainless steel as the substrates. The conditions used for these depositions are summarized in Table 2.

Table 2.2: Optimized deposition parameters for producing the final surfaces.

Assay	Subs. Thick.(μm)	Strain (%)	Substrate	Target	Conditions	
					Cleaning	**Deposition**
AJ_6 (on the grid)	800	10	PDMS	PTFE	Pressure=0.7 Pa Power=100 W D=0.002546 W/mm^3 t=5 min	Pressure=1.3 Pa Power=150 W D=0.00382 W/mm^3 t=15 min
AJ_7 (on the grid)				PA	Pressure=0.7 Pa Power=50W D=0.001273 W/mm^3 t=5 min	Pressure=1.3 Pa Power=60 W D=0.001528 W/mm^3 t=25 min
AJ_8 (on the substrate holder)	-	0	Glass, silicon, 316L	PTFE	Pressure=0.7 Pa Power=100 W D=0.002546 W/mm^3 t=5 min	Pressure=1.3 Pa Power=150 W D=0.00382 W/mm^3 t=15 min
AJ_9 (on the substrate holder)				PA	Pressure=0.7 Pa Power=50 W D=0.001273 W/mm^3 t=5 min	Pressure=1.3 Pa Power=60 W D=0.001528 W/mm^3 t=25 min

2.2 Topographic and Morphologic Characterization

2.2.1 Infinite Focus Microscopy (IFM)

Infinite Focus is an optical 3D micro coordinate system for form and roughness measurement. It combines the low depth of field of an optical microscope with vertical scanning, traversing across the surface of the sample, to provide high resolution and high depth of field topographical images with a large field of view. Its results achieve a vertical resolution of up to 10 nm and ensure repeatable accuracy [66, 67].

The Alicona Infinite Focus Light Microscope was used for this analysis, which made it possible to obtain the roughness parameters of the surface, as well as the wrinkles profile form, enabling the determination of the wavelength (λ) and amplitude (A) in different positions of the surface.

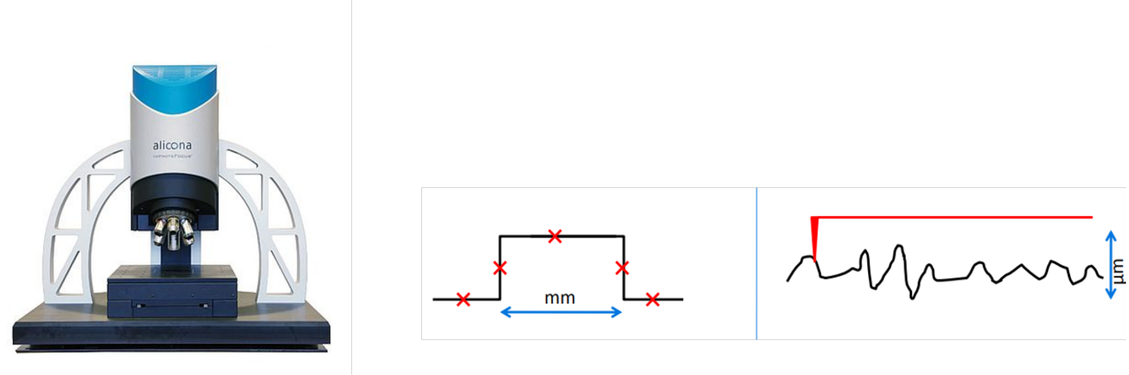

Figure 2.1: Alicona Infinite Focus Light Microscope. Scheme of form and roughness measurements [66].

2.2.2 Atomic Force Microscopy (AFM)

The AFM is a variation of high resolution scanning probe microscopy (SPM) that enables the study of the topography of non-conductive surfaces. A sharp tip is raster-scanned over a surface using a feedback loop to adjust parameters. The AFM does not need a conducting sample, as it uses atomic forces to map the tip-sample interaction. This way, it has the advantage of imaging almost any type of surface, including polymers, ceramics, composites, glass, and biological samples [68].

AFM has a feedback loop that uses the laser deflection to control the force and tip position. A laser is reflected from the back of a cantilever that includes the AFM tip. As the tip interacts with the surface, the laser position on the photodetector is used in the feedback loop to track the surface for imaging and measuring.

This technique can operate in static mode (or contact mode) or dynamic mode. In the contact mode, the tip is dragged across the surface and the surface topography is measured using the deflection of the cantilever directly or using the feedback signal required to keep the cantilever at a constant position. The dynamic mode comprises the non-contact mode and the tapping mode (Figure 3.6). In the non-contact mode, the cantilever oscillates quite close to the sample, but not touching it. Changes of the resonant frequency or amplitude of the cantilever are measured as the interaction between the tip and sample dampen the oscillation [69]. In the tapping mode, the cantilever uses a piezoelectric element mounted on the top to oscillate it near to its resonance frequency. The forces cause the amplitude to decrease as the tip gets close to the surface, and the height of the cantilever adjusts to keep the amplitude constant. The surface topography is determined by variations in amplitude and phase that characterize the cantilever vibration frequency. This tapping results in less damage to the sample than contact mode [70].

In the present work, a diInnova AFM, from Veeco Instruments Inc., was used in tapping mode with a silicon tip (Bruker) with a resonance frequency (f0) of 150 kHz and a spring constant (k) of 10 $N.m^{-1}$. The images treatment was done through the Gwyddion® program.

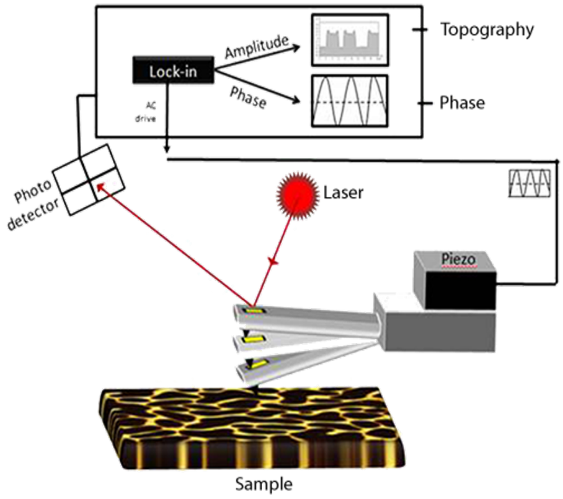

Figure 2.2: Schematic of dynamic AFM mode operation [69].

2.2.3 Scanning Electron Microscopy (SEM)

The scanning electron microscope (SEM) uses a focused beam of high-energy electrons to generate a variety of signals at the surface of solid samples. The signals that derive from electron-sample interactions reveal information about the sample including external morphology, chemical composition, and crystalline structure and orientation of materials making up the sample [71].

Electrons are produced at the top of the column, accelerated down and passed through a combination of lenses and apertures to produce a focused beam of electrons which hits the surface of the sample. The position of the electron beam on the sample is controlled by scan coils situated above the objective lens. These coils allow the beam to be scanned over the surface of the sample, collecting information about this area. As the electrons interact with the sample, they produce secondary electrons, backscattered electrons and characteristic X-rays.

These signals are then detected by appropriate detectors [72] (Figure 3.5). Secondary electrons are most valuable for showing the morphology and topography of the samples whereas backscattered electrons contribute for illustrating composition contrasts in multiphase samples [71].

When the sample has a low electrical conductivity, it is usually covered with a nanomaterial layer of palladium/gold.

For this technique 3 equipments were used: (i) Philips XL30, which uses tungsten filament as the electron source; (ii) FEI Quanta 400FEG ESEM, where the electron beam is generated using a Field Emission Gun (FEG); (iii) ZEISS Merlin GeminiSEM, which also uses FEG.

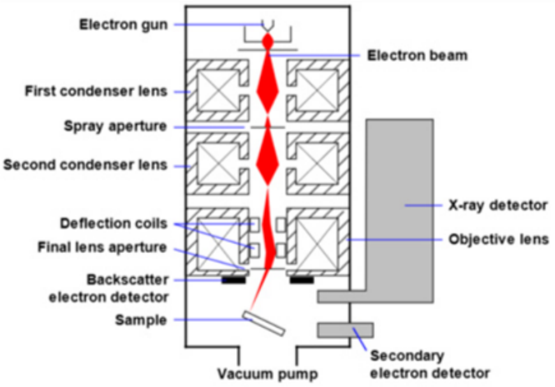
Electron gun
Electron beam
First condenser lens
Spray aperture
Second condenser lens
X-ray detector
Deflection coils
Objective lens
Final lens aperture
Backscatter electron detector
Sample
Secondary electron detector
Vacuum pump

Figure 2.3: Scheme of a scanning electron microscope [72].

2.3 Structural Characterization

X-ray diffraction (XDR) is one of the main techniques of microstructural characterization of crystalline materials. X-ray diffraction is based on constructive interference of monochromatic X-rays and a crystalline sample, which has a structure composed of atoms organized in well-defined planes and distances between them.

The X-rays are generated by a cathode ray tube, filtered to produce monochromatic radiation, collimated to concentrate, and directed toward the sample. When Bragg's Law ($n\lambda = 2d\sin(\theta)$) is satisfied, x-rays scattered by the atoms in the plane of a periodic structure are in phase and diffraction occurs in the direction defined by the angle θ . In this equation, n is an integer that represents the order of the diffraction, λ is the characteristic wavelength of the X-rays impinging on the crystallize sample, d is the interplanar spacing between rows of atoms, and θ is the angle of the x-ray beam with respect to these planes. By scanning the sample through a range of 2θ angles, all possible diffraction directions of the lattice should be attained due to the random orientation of the material. The chemical identification can be performed by comparing this diffraction pattern to a database of known patterns [73, 74].

In this study, X'Pert equipment with Copper target ($K\lambda\alpha 1 = 0.15418$ nm), from PanAlytical, was used, with a voltage of 45 kV, a current of 40 mA, a scanning range of 10 to 60°, with a step of 0.03° and a time of 1 s/step.

2.4 Chemical Characterization

Fourier transform infrared (FTIR) is the preferred method of infrared spectroscopy. When a material is irradiated with infrared radiation, absorbed IR radiation usually excites molecules into a higher vibrational state. The wavelength of light absorbed by a particular molecule is a function of the energy difference between the at-rest and excited vibrational states. The wavelengths that are absorbed by the sample are characteristic of its molecular structure [75].

In FTIR spectroscopy, radiation containing many frequencies of light is passed through a sample; some radiation is absorbed by the sample and some is transmitted. The beam is then modified to contain a different combination of frequencies and this process is repeated many times. The signal obtained from the detector is an interferogram, which must be analyzed with a computer using Fourier transforms to turn the raw data into the desired result (light absorption for each wavelength). From this analysis results a representation of the molecular 'fingerprint' of the sample, as it enables to identify the different functional groups present [76]. This technique allows the measurement of even large sample areas with a very high lateral resolution within a few minutes.

The equipment used was the Perkin Elmer Frontier Spectrometer (FT-NIR / MIR), equipped with a FR-DTGS detector and a KBr beam splitter. The recording of the spectra was performed with 4.0 cm^{-1} resolution with 16 accumulations and using the Non-Destructive Attenuated Total Reflectance (ATR) sampling technique.

2.5 Wettability

The wettability of a surface can be determined by the static contact angle (θ) measured between the material surface and a liquid of a certain polarity. This contact angle is the result of the mechanical equilibrium of a drop resting on a plane solid surface under the action of three surface tensions – γ_{LV} at the interface of the liquid and vapor phases, γ_{SL} at the interface of the solid and the liquid, and γ_{SV} at the interface of the solid and vapor (Figure 2.4) – and it can be described by the Young's equation represented below [77].

$$\gamma_{LV}\cos(\theta) = \gamma_{SV} - \gamma_{SL} \tag{2.1}$$

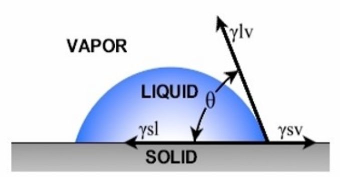

Figure 2.4: Contact angle of a sessile drop.

A low contact angle between the material and the liquid indicates good spreading on the surface, i.e. hydrophilicity of the material, while a high contact angle is a characteristic of hydrophobic surfaces. According to Vogler, evidence from more than a decade of intermolecular force research on biomaterials interaction suggests that hydrophobic surfaces exhibit water contact angles greater than 65°, whereas hydrophilic surfaces exhibit water contact angles below 65° [27]. The equilibrium described by Young's equation is only true for ideally smooth and homogeneous solid surfaces. However, real surfaces do not have perfect smoothness, rigidity, or chemical homogeneity. Such deviations from ideality result in contact-angle hysteresis, which is defined as the difference between the advancing (θ_a) contact angle (the maximum stable angle) and the receding (θ_r) contact angle (the minimum stable angle) (Figure 2.5). This phenomenon happens because many different stable contact angles are found on a non-ideal solid [78].

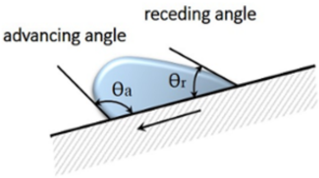

Figure 2.5: Schematic of advancing and receding contact angles [79].

In an attempt to describe wettability of rough texturized surfaces, Wenzel and Cassie–Baxter developed two models. Wenzel theory assumed that a rough surface extends the solid-liquid interface area, with the liquid filling in the grooves of the surface (Figure 2.6). This model has been found to be useful in surfaces of well wettability ($0° < \theta < 90°$) and simple topography [80]. The contact angle for this model can be determined by the following equation:

$$\cos(\theta^*) = r\cos(\theta) \tag{2.2}$$

In this equation θ^* is the angle on the roughness-free surface, r is the roughness factor defined as the ratio of the current surface area to the projected surface area and θ is the contact angle measured experimentally.

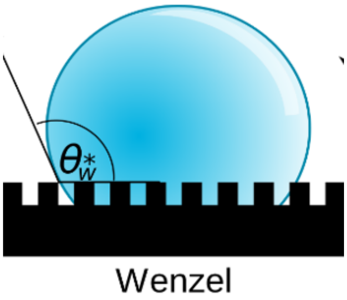

Figure 2.6: Schematic representation of the Wenzel model.

However, when the contact angle lies in the range 90° $< \theta <$ 180°, the liquid does not penetrate well through the grooves and gas molecules can be trapped in the valleys. As a result, the interface between liquid and solid is not continuous and there is an alternation of solid-liquid and gas-liquid interfaces (Figure 2.7) [80]. This is the assumption followed by the Cassie and Baxter model, which determines the apparent contact angle for a composite material by the equation:

$$\cos(\theta^*) = f\cos(\theta) - 1 + \theta, \tag{2.3}$$

where f is the fraction of the surface with which the liquid comes into contact.

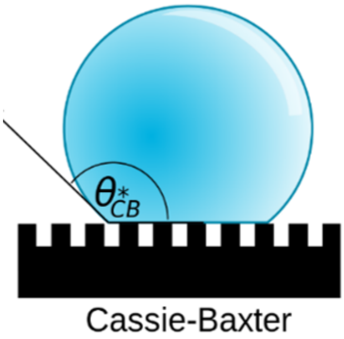

Figure 2.7: Schematic representation of the Cassie and Baxter model.

The surface energy plays an important role in any surface interaction between a polymer and a fluid. It will determine the degree of wetting, the facility with which fluids can penetrate into fibrillated regions, and, to some extent, the energetics of fluid–polymer interactions. It acts to minimize the free surface of a material and controls many interfacial properties. The measurement of the contact angles can also be used to determine the surface energy of a material. If the surface energies of liquid and surface are similar, the contact angle will be low and wetting will occur.

If the surface energies are dissimilar, the contact angle will be large and beading will occur [81]. The following equations allow the determination of the surface tension of a surface, as well as its polar and dispersive components:

$$\gamma_s = \gamma_S^d + \gamma_S^p, \tag{2.4}$$

$$\gamma_s(1 + \cos(\theta)) = 2\sqrt{\gamma_S^d \gamma_L^d} + 2\sqrt{\gamma_S^p \gamma_L^p}, \tag{2.5}$$

, where θ is the static contact angle measured for each liquid, γ_s is the surface tension of the film, γ_S^d is the dispersive component of the surface tension, γ_S^p is the polar component of the surface tension, γ_L is the surface tension of the liquid, γ_L^d is the dispersive component of the of the liquid surface tension and γ_L^p the polar component of the of the liquid surface tension [28, 82].

In this work, the static contact angles were measured by placing a drop of 10 μL of distilled water or formamide on the surfaces. A posterior determination of the contact angle value was done through the DataPhysics QCA-20 equipment. Seven measurements were performed on each surface and the results are presented as mean values.

2.6 Surface Charge

The study of the zeta potential (ζ) for biomedical applications is very important because once they are introduced in the organism they will become subjected to different types of fluids. The charge at the material surface attracts counterions on the fluid which will neutralize the charge. These ions close to the interface are strongly attached to the surface and form an inner layer known as Stern layer. After this layer, and as the distance increases, the attachment will lose strength, and a diffuse layer consisting of both same and opposite charged ions/molecules grows. The composition of this diffuse layer depends on a variety of factors such as pH, ionic strength and electrolyte concentration [83]. When an electric field is applied to such dispersion, the charged particles move towards the opposite electrode and the zeta potential is the electrokinetic potential at the interface between the mobile particles and dispersant (slipping plane) (Figure 2.8). The zeta potential characterizes the distribution of electrical charges on the surface and its magnitude gives an indication of the potential stability of the colloidal system.

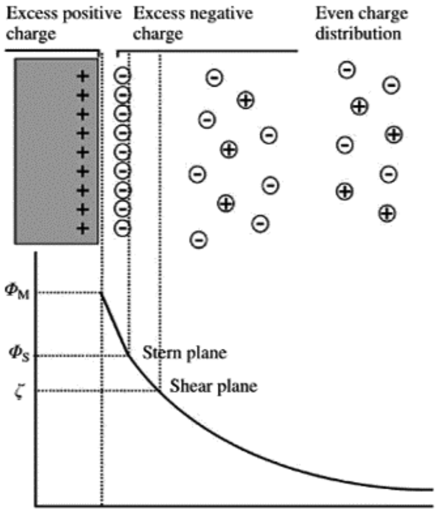

Figure 2.8: Representation of the double layered developed on a particle suspended in a dispersion medium [84].

The equipment used to measure the zeta potential of the surfaces was the SurPASS, from Anton Paar GmbH, and the electrolyte used was a solution of 1 mM KCl with pH 7 and the clamping cell. The determinations were made using the clamping cell mode.

2.7 Mechanical Characterization

The mechanical properties of polymers are characterized by the way they respond to the mechanical solicitations. The nature of this response depends on the chemical structure, temperature, time and the processing conditions of the polymer. Due to their chemical nature polymers present a viscoelastic behavior. When an elastic material is stressed, there is an immediate and corresponding strain response and when the stress is removed the strain returns to zero (Figure 2.9 a,b). As the solicitation is made in the elastic region, the applied stress σ is directly proportional to the strain ε and can be described by Hooke's law:

$$\sigma = E\varepsilon, \tag{2.6}$$

where E is the Young's modulus of the material.

When stress is applied on a viscous fluid it will deform permanently and continues to deform if stressed again (Figure 2.9a,c). This behavior can be described by Newton's Law.

$$\sigma = \eta\frac{d\varepsilon}{dt}, \tag{2.7}$$

where η is the viscosity of the fluid and $\frac{d\varepsilon}{dt}$ is the rate of shear strain.

In a viscoelastic material such as a polymer, its deformations under stress are time dependent. If the stress is held constant, then the resultant strain will increase with time, i.e. the polymer creeps. If a constant deformation is imposed, then the induced stress will relax with time (stress relaxation). Usually, the polymer remains with a permanent deformation . (Figure 2.9a,d) [85].

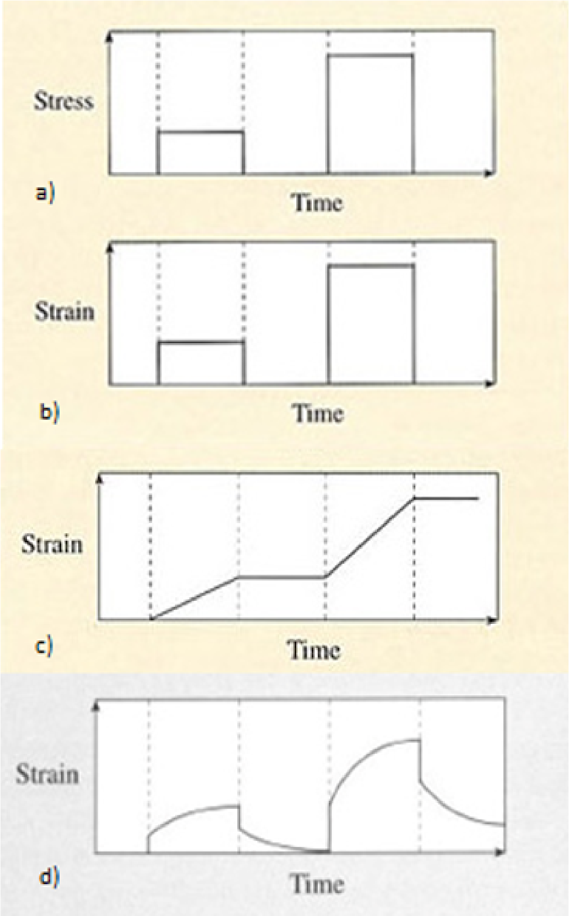

Figure 2.9: Representation of (a) stress applied to a material over time and the strain response in case of (b) an elastic material, (c) viscous fluid or (d) viscoelastic material. Adapted from [85].

2.7.1 Tensile test

The tensile test output is usually a stress-strain diagram (Figure 2.10) and several mechanical properties can be determined, such as: the elastic, or Young's, modulus (E), elongation and tensile strength (at yield and at break). The elastic modulus is a measure of the stiffness of the material, but it only applies in the linear region of the curve (which respects Hooke's Law). This point is called the elastic limit. From this point on in the tensile test, the material reacts plastically to any further increase in load, which means that it will not return to its original state once the load is removed [86].

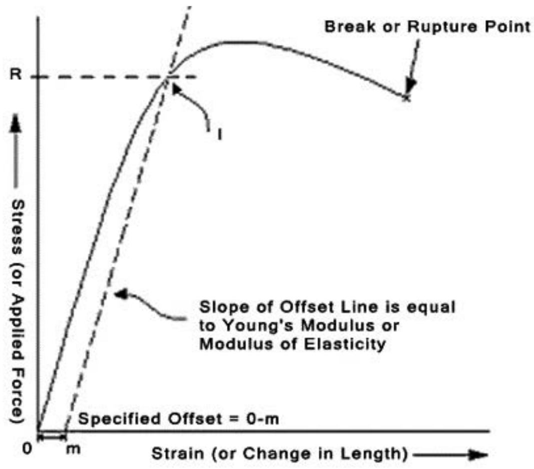
Break or Rupture Point
R
I
Stress (or Applied Force)
Slope of Offset Line is equal to Young's Modulus or Modulus of Elasticity
Specified Offset = 0-m
0
m
Strain (or Change in Length)

Figure 2.10: Stress-strain curve obtained from a tensile test [86].

For the tensile tests, the Autograph AGS-1kNX model from Shimadzu and the TRAPEZIUM X program were used (Figure 2.11). The PDMS samples had to be secure with help of small polyvinyl chloride (PVC) structures on the extremities. The test was performed with a velocity of 5 mm/min.

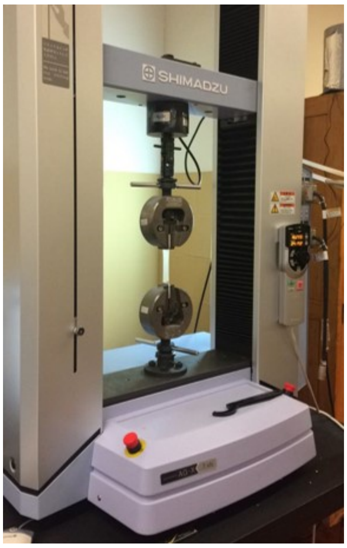

Figure 2.11: Autograph AGS-1kNX model from Shimadzu. Photo taken during the tensile tests.

2.7.2 Stress relaxation test

The stress relaxation test involves straining a material at constant strain and then holding that strain (Figure 2.12). The stress required to hold the viscoelastic material at the constant strain will be found to decrease over time due to a re-arrangement of the material on the molecular and micro-scale [87, 88].

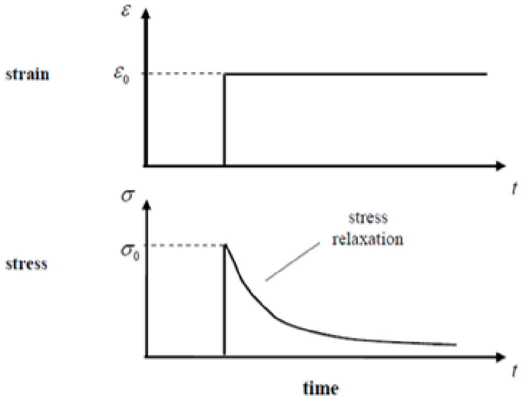

Figure 2.12: Typical stress response of a viscoelastic material to the stress-relaxation test [89].

The relaxation time (τ), which is characteristic of each polymer at a certain temperature, can be determined by the following equation:

$$\sigma = \sigma_0 exp\left(\frac{-t}{\tau}\right), \tag{2.8}$$

where σ is the final stress, σ_0 is the initial stress and t is the time (in hours).

For the stress relaxation test, the Autograph AGS-1kNX model from Shimadzu and the TRAPEZIUM X program were used. The test was performed with a velocity of 7.5mm/min and 27% of initial strain was applied.

2.7.3 Cyclic test

The cyclic test involves a repeating pattern of loading-unloading. It can be strain-controlled (observing the resulting stress), as in Figure 2.13, or stress-controlled (observing the resulting strain). The results of a cyclic test can be quite complex, due to the creep, stress-relaxation and permanent deformations.

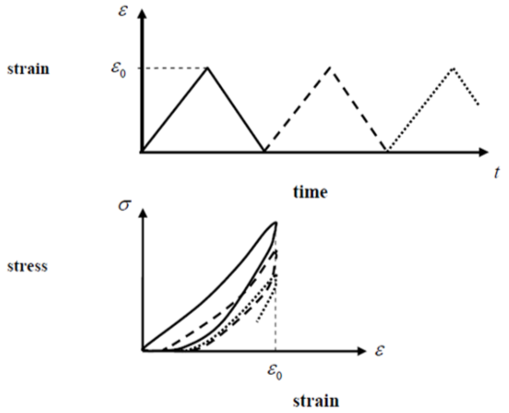

Figure 2.13: Typical stress response of a viscoelastic material to the cyclic test [89].

The typical response of a viscoelastic material is sketched in Figure 2.13. It is observed that the loading and unloading curves do not coincide and, instead, a hysteresis loop is formed, which is a measure of the energy lost through heat transfer mechanisms during the deformation [89].

The Autograph AGS-1kNX model from Shimadzu and the TRAPEZIUM X program were again used for performing the cyclic tests. 10 cycles were made until reaching 20% of sample strain, with a velocity of 7.5mm/min.

2.8 Tests *in vitro*

Along this subsection, PDMS is used to designate the PDMS samples without any coating, PDMS/PT correspond to the PDMS samples with the PTFE wrinkling film and PDMS/PA are the PDMS samples with the PA wrinkling film. All three type of surfaces were tested in vitro with the purpose of studying cell behavior in function of the chemical and physical properties of the surfaces.

For these tests, Human Umbilical Cord Mesenchymal stem cells (hUC-MSCs), obtained from PromoCell, Cat. C-12971; Lot No. 1112304.2, were used. Firstly, cell viability was assessed by absorbance spectroscopy, measuring cells proliferation, and SEM analysis was performed. The MSCs $[ca^{2+}]$i was determined by epifluorescence technique to assess the cells ability to expand and survive. Finally, the samples capacity to promote and/or inhibit MSCs osteogenic differentiation was determined.

Statistical analysis was performed using the GraphPad Prism version 6.00 for Mac OS X, GraphPad Software, La Jolla California USA. The experiments were performed in quadruplicates and the results were presented as Mean ± Standard Error of Mean (SD). Analysis was performed by one-way ANOVA analysis, and Tukey's multiple comparisons test. Differences were considered statistically significant at $p \leq 0.05$.

2.8.1 In vitro cell viability assessment

a) Sample Sterilization

All membranes were pre-sterilized with 75% ethanol and irradiated with UV light for 20 minutes in each side.

b) Cell culture and maintenance

hUC-MSCs were maintained in DMEM, GlutaMAX^{TM} Supplement, no nucleosides (Gibco, 21885-025) supplemented with 10% (v/v) fetal bovine serum (FBS) obtained from BI, Biological Industries (BI LTD, Certified FBS, ref$*$04-400-1A), 100 IU/mL penicillin, 0.1 mg/mL streptomycin (Gibco, 15140122), 2.05 μg/mL Amphotericin B (Gibco, 15290026) and 10mM HEPES Buffer solution (Gibco, 15630122). FBS is heat inactivated, sterile-filtered, and according to the manufacturer information, presents Hemoglobin in a concentration $\leq$25 mg/dL, and $\leq$10 EU/mL endotoxin. All cells were maintained at 37°C and 95% humidified atmosphere with 5% CO_2 environment.

c) Presto Blue Cell Viability Assay

Cell viability assessment is based on cell permeability to a resazurin- based solution that functions as a cell viability indicator because it uses the reducing power of living cells to quantitatively measure the proliferation of cells.

PDMS, PDMS/PT and PDMS/PA were tested for their cytocompatibility towards hUC-MSCs by incubating them in a 24 multiwell and seeded with 12,000 cells per well. Control wells were seeded with same cell density. Cells were left to adhere at 37°C, in a 5% CO_2 atmosphere.

At every time point (24 hours (1 day), 72 hours (3 days), 120 hours (5 days) and 168 hours (7 days)) culture medium was removed from each well and fresh complete medium was added, with 10% (v/v) of 10x Presto Blue cell viability reagent (Invitrogen, A13262) for 1 hour at 37°C, in a 5% CO2 atmosphere. Changes in cell viability were detected by absorbance spectroscopy in a Thermo Scientific Multiskan FC. Supernatant was collected and transferred to a 96 well plate, absorbance was read at 570 nm and 595 nm and the corrected absorbance was determined. After, cells were washed with Phosphate buffer solution (DPBS, Gibco, Life Technologies) to remove any Presto Blue residues and fresh culture medium was reset to each well.

d) SEM

After completion of cell viability tests, the surfaces seeded with hUC-MSCs, were collected and washed three times with 0.1M HEPES buffer (Merck®, PHG0001). Cells were fixated with 2% buffered glutaraldehyde (Merck®, G7651), overnight. Afterwards, cells were rinsed with 0.1M HEPES buffer three times, for 5 minutes each, with gentle agitation. Samples were then dehydrated in crescent concentration of ethanol.

Chemical drying with Hexamethyldisilazane (HMDS) (Merck®, 440191) was further performed in some samples. Briefly, cells were incubated with increasing concentrations of HMDS in ethanol for 15 minutes and finally with HMDS alone for 15 minutes. After removing the HMDS from each well, samples were left to evaporate in a fume hood.

Subsequently, some of the samples were coated with an Au/Pd thin film, by sputtering, using the SPI Module Sputter Coater equipment. The SEM exam was performed using a high resolution (Schottky) Environmental Scanning Electron Microscope with X-Ray Microanalysis and Electron Backscattered Diffraction analysis: Quanta 400 FEG ESEM / EDAX Genesis X4M in high vacuum mode.

2.8.2 Ca2+ indicator Fura-2/AM loading

The intracellular calcium concentration ([Ca^{2+}]i) was measured in Fura-2-AM-loaded cells using dual wavelength spectrofluorometry as previously described by Fisher and colleagues [90]. The common fluorescent indicators for Ca^{2+} are polycarboxylate anions that cannot cross lipid bilayer membranes and therefore are not cell permeant. hUC-MSCs (cultured on PDMS, PDMS/PT and PDMS/PA membranes, and without biomaterial – cells alone (control), in standard culture medium and osteogenic culture medium) were loaded with Ca^{2+} indicator by incubation in 2.5 mM Fura-2 acetoxymethyl ester (Fura-2-AM, Molecular Probes) and 0.03% Pluronic (Molecular Probe) in a Ringer Solution with the following composition: 121 mM NaCl, 5.4 mM KCl, 9 mM D-glucose, 1.5 mM MgCl2, 1.8 mM CaCl2, 6 mM NaHCO3, and 25 mM HEPES, with a pH of 7.4; at 37°C in darkness for 120 minutes.

After loading Fura-2-AM, hUC-MSCs were washed in Ringer Solution. The wells presenting adhering MSCs cells in PDMS, PDMS/PT and PDMS/PA membranes and the control wells from the two experimental groups (in standard culture medium and osteogenic culture medium) were transferred to a glass chamber containing 100 μl of the Ringer Solution. The chamber was placed in a well on the stage of an epifluorescence microscope (Zeiss, Germany). Fluorescence measurements were performed in each individual cell.

The emitted fluorescence intensities at 510 nm were acquired by computer software, which registered the number of photons emitted per second, during 30 s for each 340 nm and 380 nm excitation wavelengths. The $[Ca^{2+}]$i was estimated from the ratio equation described by Grynkiewiez and colleagues [91]. For determination background fluorescence, cells were incubated in 2.5 mM 4-br-A23186 (Molecular Probe) and 10 mM MnCl2 in 100 μl of Ringer solution at room temperature in darkness for 10 minutes. The $[Ca^{2+}]$i measurements considered for these results were the ones which background signal was inferior to 20% of the total emitted fluorescence. 25 MSCs cells were analyzed per experimental well.

2.8.3 Osteogenic differentiation assay

PDMS, PDMS/PT and PDMS/PA were evaluated in their capacity to promote and or inhibit osteogenic differentiation in hUC-MSCs. The samples were incubated in a 24 multiwell and seeded with 20,000 cells per well. Control wells were seeded with same cell density. Cells were left to adhere at 37°C, in a 5% CO_2 humidified atmosphere until 70-80% confluence was reached (after 3 days). At this point, in each well a specific formulated Osteogenesis media, composed of expansion media further supplemented with 5nM Dexamethasone (D8893 – Sigma Aldrich®), 250 μM de ascorbic acid-2- phosphate (A4403, Sigma Aldrich®) e 10mM β-glycerophosphate (β-GP, G9422, Sigma Aldrich®) was added. Control samples were maintained in culture media absent on osteogenic supplements. The media was changed every 3 days, for 21 days. After this period, Alizarin Red S (ARS) assay was used to qualitatively and semi-quantitatively determine Osteogenic differentiation of hUC-MSCs [92]. For this purpose, culture media was removed, wells were abundantly washed with DPBS (14190- 094, Gibco®) and cells were fixed with 4% formaldehyde for 20 minutes. After removal of the fixation agent, the samples washed with diH2O and 40 mM ARS (2003999, EMD Millipore Corporation®) was added to each well and incubated for 30 min with gentle shaking. Following incubation, unbound dye was removed and samples washed with diH2O until supernatant became clear. The multiwells were left to completely dry and then stored at -20°C until dye extraction. For extraction and quantification of ARS, samples were incubated with 10% acetic acid (537020, Sigma Aldrich®) for 30 min, with gentle shaking. After incubation, cells and mineral deposits were scraped from the plate and collected, heated at 85°C for 10 minutes and immediately transferred to ice, for 5 minutes. The samples were centrifuged, and individual absorbance values were measured at 405 nm in a Thermo Scientific Multiskan FC plate reader (Ref. 51119000), along with a standard curve for the calculation ARS concentration (μM).

3

Results and Discussion

3.1 Preliminary Studies

A first phase was performed with the goal of studying the influence of the substrate thickness and the use of mechanical strain onto the deposited film topography.

The optical micrographs (Figure 3.1) show that wrinkles were formed in all the PDMS substrates submitted to the PTFE deposition. This was expected because the temperature increases continually during the plasma cleaning and the deposition, which causes the substrate to expand during the deposition of the coating. However, when the process is over, the substrate returns to its original form as the temperature decreases, and the deposited thin film wrinkles due to tensions created between the two polymers [28].

This wrinkling topography presents a random distribution, although affected by the substrate thickness. As seen in Figure 3.1b,c, wrinkles adopted a more linear pattern on the 400 μm thick PDMS substrate, unlike the one with thickness of 1000 μm , where wrinkles appeared in a more random distribution.

The PDMS substrates strained prior to the deposition (Figure 3.1d,e) presented wrinkles oriented perpendicularly to the direction of the applied force. This approach suggests a more stable/efficient manner to control the orientation of the wrinkles than using different substrate thicknesses. Straining to 10% deformation showed to be enough for the aligned wrinkly pattern formation (Figure 3.1d). Also, on the samples strained with 15 and 30% deformation, the substrates appeared to be damaged as a result of the overstraining (Figure 3.1e).

From this preliminary analysis, and since an aligned topographical structure has been shown to strongly influence cell guidance and tissue morphogenesis [49,50], the remaining experimental work was developed using PDMS substrates strained with 10% deformation prior to the depositions. Concerning the substrate thickness, a value of 800 μm was chosen, as PDMS revealed to be difficult to handle, especially when preparing and straining very thin samples. Thus, as wrinkles were successfully obtained on 400 μm, 800 μm and 1000 μm thick substrates, 800 μm was the chosen thickness.

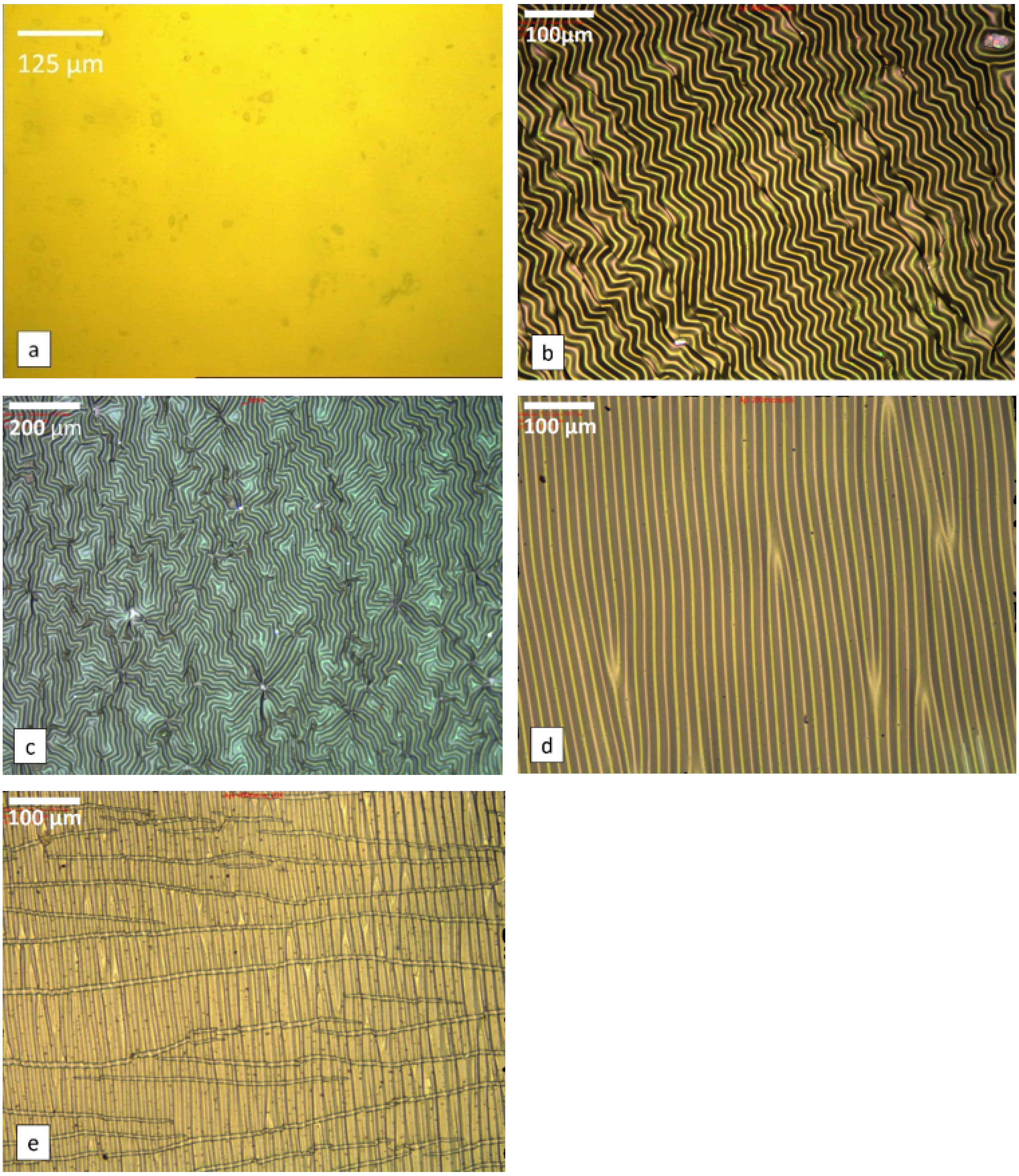

Figure 3.1: Optical micrographs of PTFE deposited thin films onto PDMS: (a) 100 μm thick PDMS sample; (b) 400 μm thick PDMS without previous deformation, (c) 1000 μm thick PDMS without previous deformation; (d) 400 μm thick PDMS with 10% previous deformation; (e) the 400 μm thick PDMS with 15% previous deformation.

In the final depositions, PTFE and PA were sputter deposited onto PDMS substrates 10% strained. These depositions were repeated a few times in order to obtain several samples with wrinkles on the transversal and longitudinal directions

(Figure 3.2).

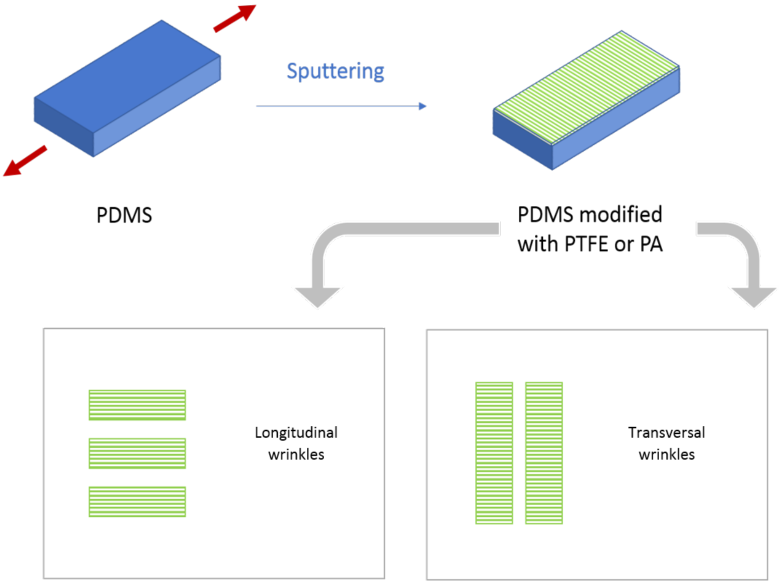

Figure 3.2: Schematic representation of the approach followed to create transversal and longitudinal wrinkling patterns on the PDMS surface.

3.2 Topographic and Morphologic Characterization

The use of different polymers as targets had the purpose of creating films with distinct chemical properties. However, when comparing both surfaces it is readily noticeable that the chemical composition is not the only factor differing, because the topography also changes (Figure 3.3). As expected, both films present wrinkles perpendicular to the applied deformation direction. However, the PA film (Figure 3.3c,d) presents much thinner wrinkles than the PTFE film (Figure 3.3a,b). An explanation for this can be the use of a lower power in the PA deposition which cause the temperature to increase less than in the PTFE deposition and, consequently, the substrate expansion is smaller. Ultimately, the use of different materials as targets causes differences in the films topography.

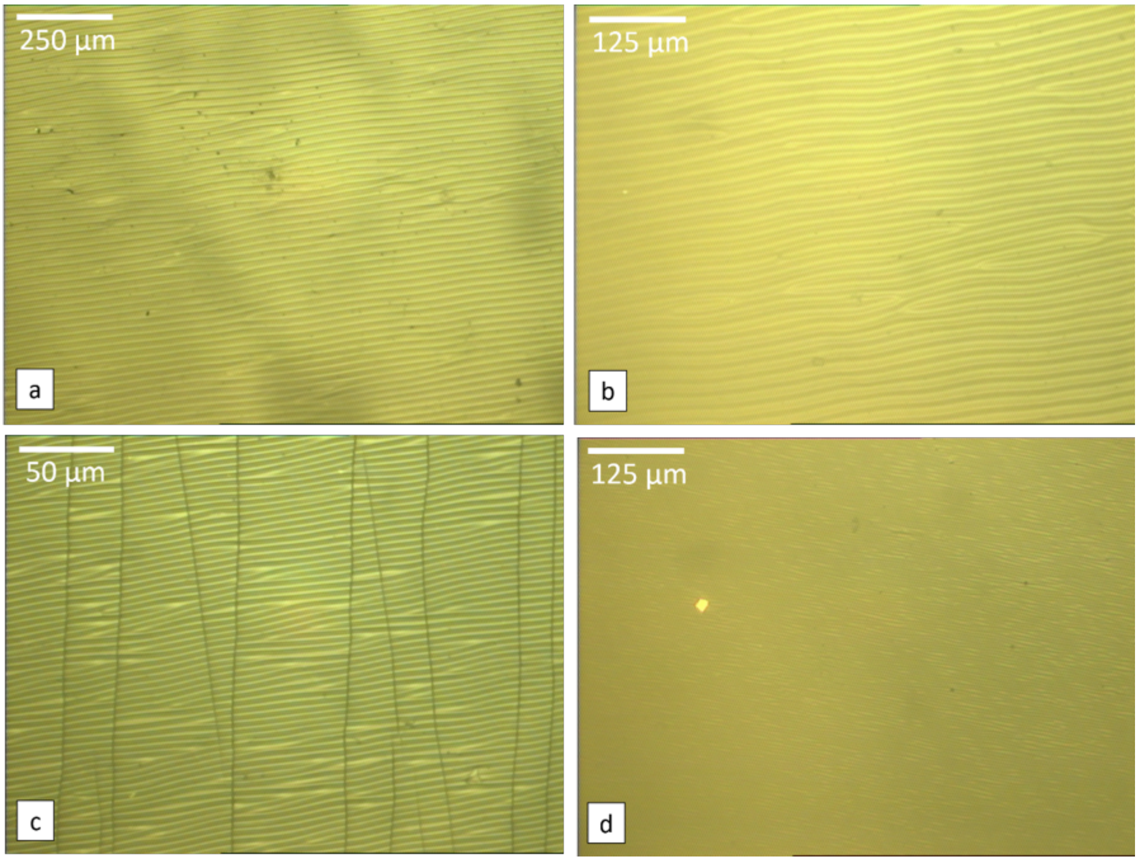

Figure 3.3: Optical micrographs of the PDMS substrates after the deposition of: (a, b) a PTFE thin film; (c, d) PA thin film.

IFM analysis was performed to determine the wrinkles profile form (Figure 3.4), enabling the determination of the wavelength (λ) and amplitude (A) in different positions of the surface, as well as the roughness parameters of the surface (Table 3.1). As previously seen on the optical micrographs, the wrinkles on the PA film present values of wavelength and amplitude considerably smaller than the ones on the PTFE film.

The surface average roughness of profile, Sa, represents the arithmetic average of the absolute values of the profile heights over the evaluated area. The surface root-mean-square roughness of profile, Sq, is the standard deviation of the distribution of surface heights. Smax is defined as the vertical distance between the highest peak and the lowest valley along the analyzed area. Skewness (skew) is a measure of the asymmetry of the profile which implies that the number of valleys is, in average, equal to the number of peaks, this dimensionless parameter is zero. A negative skewness indicates predominance of peaks and a positive value indicates that valleys predominate. At last, kurtosis describes the sharpness of the profile. If this value is less than 3 the distribution curve is said to be platykurtic and has relatively few high peaks and low valleys. On the other hand, if the kurtosis is above

3 the distribution curve is said to be leptokurtic and has relatively many high peaks and low valleys [93].

Comparing the roughness parameters for both surfaces, Sa, Sq and Smax values are higher for the PTFE film, which was expected because these depositions were done with higher deposition power, resulting in wrinkles with increased dimensions. The skewness parameter shows that the PA film is more symmetric between valleys and peaks, and that the PTFE film profile presents a height distribution skewed above the mean plane. Both surfaces have a kurtosis value above 3, which corresponds to a more "sharped" distribution.

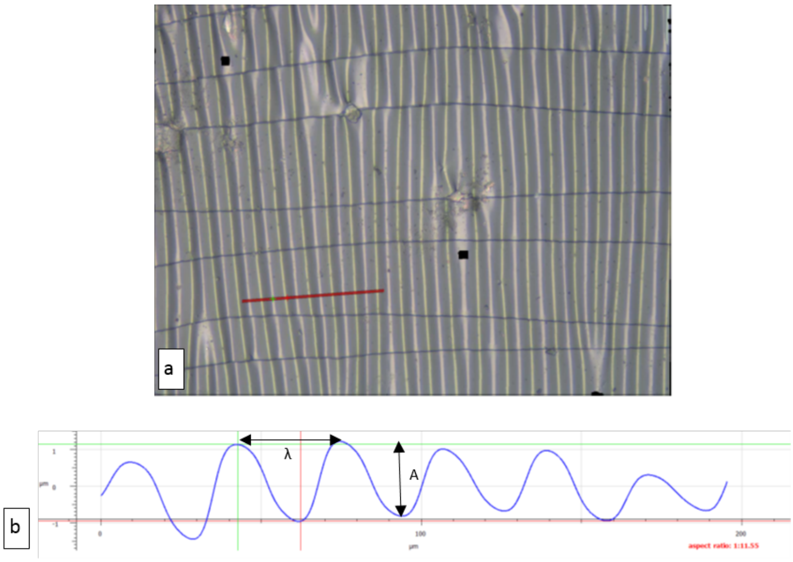

Figure 3.4: IFM analysis of AJ_6 thin film. Representation of the 2D roughness profile for wavelength and amplitude evaluation (b) from the position indicated by the red line in (a).

Table 3.1: Amplitude and wavelength of the wrinkles on the PTFE and PA films deposited on PDMS, as well as roughness parameters determined through IFM analysis.

Film	$A \pm \delta A$ (μm)	$\lambda \pm \delta\lambda$ (μm)	**Sa** (μm)	**Sq** (μm)	**Smax** (μm)	**Skew**	**Kurtosis**
PA	0.17±0.05	6.45±0.53	0.063	0.082	0.610	-0.003	4.201
PTFE	2.29±0.32	32.19±0.56	0.774	1.012	7.484	0.867	4.710

The morphology of the surfaces, both at a micro- and nanometer level, was characterized by SEM (Figure 3.5). The PTFE surface presents wrinkles both at the microscale (Figure 3.5a) and also at the nanoscale (Figure 3.5b,c). The reason for this lays on the fact that the PTFE chain, which is a long and linear fluorocarboned structure, during the sputtering process, splits and small agglomerates of 3 or 4 atoms are ejected from the target. When these groups of atoms reach the substrate they don't present a great mobility and don't diffuse along the surface, instead they nucleate on the location of arrival. They experience growth with the incoming material and then aggregate with their neighbors, in order to minimize surface energy, constituting the roughness at the nanolevel. The resulting PTFE based coating presents a more crosslinked structure when compared to the linear structure of the PTFE target. The wrinkles at the microscale, as already mentioned before, were formed due to temperature variations at the time of the deposition and the differences between the thermal expansion coefficients of the substrate and the film. The substrate pre-straining results in wrinkle alignment at the time of the deformation removal.

In case of the PA film, there's no nano-roughness detected, only wrinkles at the microlevel are visible (Figure 3.5d,e), which were formed by the reason already mentioned previously for the PTFE film microroughness. Also, the power used, which was higher in the PTFE deposition, certainly had an influence in the differences between the morphology of the two films.

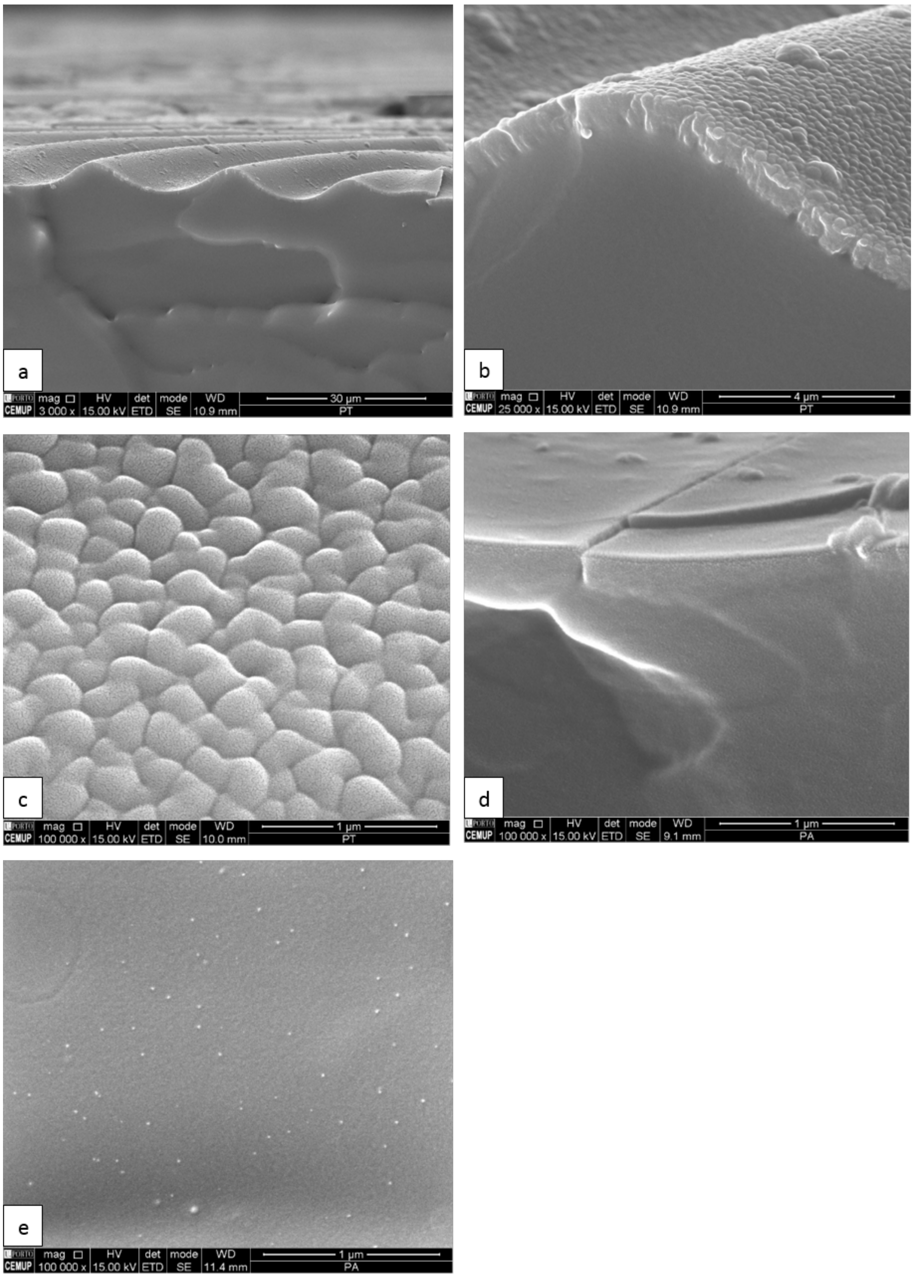
a
mag HV det mode WD
3 000 x 15.00 kV ETD SE 10.9 mm
30 µm
PT
b
mag HV det mode WD
25 000 x 15.00 kV ETD SE 10.9 mm
4 µm
PT
c
mag HV det mode WD
100 000 x 15.00 kV ETD SE 10.0 mm
1 µm
PT
d
mag HV det mode WD
100 000 x 15.00 kV ETD SE 9.1 mm
1 µm
PA
e
mag HV det mode WD
100 000 x 15.00 kV ETD SE 11.4 mm
1 µm
PA

Figure 3.5: SEM micrographs of the PTFE film (a, b, c) and the film PA (d, e) deposited onto the PDMS substrates.

The films deposited onto silicon substrates were analyzed by AFM, resulting in topographic, amplitude and phase images. As seen in Figure 3.6 and Figure 3.7, the films don't present the same topographic pattern (wrinkles) as the ones on the PDMS substrates. However, a roughness pattern can be seen for both surfaces. A hypothetical model of the fluorocarbon film, PTFE, is presented in Figure 3.8 [94].

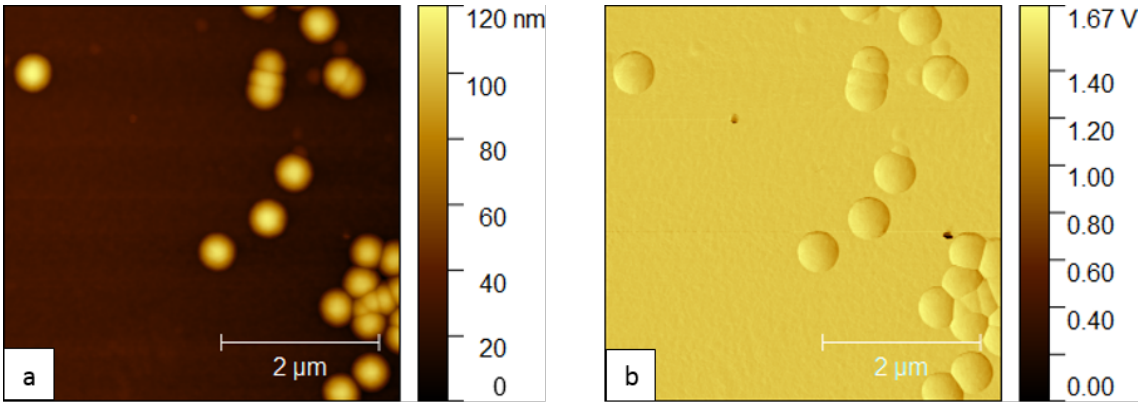

Figure 3.6: Topographic (a) and phase (b) images of the PTFE film deposited over silicon.

Observing the AFM results for the PA film on silicon (Figure 3.7) is possible to see a very subtle nano-roughness on the surface originated due to the sputtering process. The phase image reveals a nearly uniform distribution of distinct chemical groups, which can be observed by the presence of darker and lighter areas.

The roughness parameters, presented in Table 3.2, indicate, once again, that Sa and Sq values are affected by the power used during the deposition, increasing its values with the increase of power. The skewness values are in agreement with the AFM images: PA film presents a much more symmetrical profile between the peaks and valleys, contrary to the PTFE film. The value of kurtosis for the PA film surface reveals the existence of relatively few high peaks and low valleys (more flattened shape), in opposition to the PTFE film presenting a value of kurtosis above 3 (more sharped shape). The difference between the surface and the projected areas represents the area occupied by peaks and valleys.

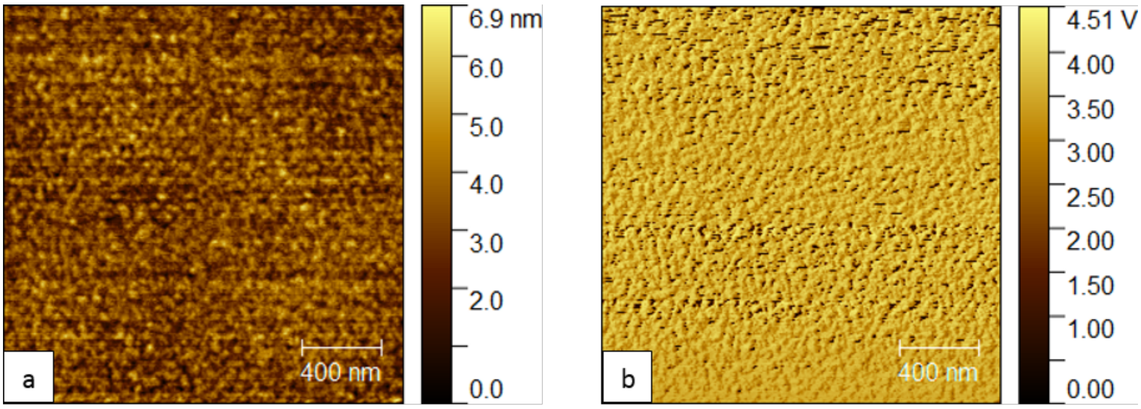

Figure 3.7: Topographic (a) and phase (b) images of the PA film deposited over silicon.

Table 3.2: Roughness parameters of the films deposited over silicon, obtained from AFM analysis.

Film	**Sa (nm)**	**Sq (nm)**	**Skewness**	**Kurtosis**	**Projected area (μm^2)**	**Surface area (μm^2)**
PTFE	10.1	17.6	2.60	6.8	25.00	25.40
PA	0.7	0.9	0.03	-31.3E-3	4.0	4.01

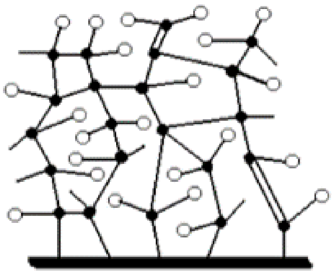

Figure 3.8: Model of fluorocarbon plasma polymer obtained by PTFE sputtering (the black dots represent carbon atoms and the white dots represent fluorine atoms). Adapted from [94].

3.3 Structural Characterization

In order obtain information concerning the structural characterization of the coatings and compare it with the target, X-ray diffraction was performed. Analyzing Figure 3.9, it is possible to see that the initial crystallinity present by the PTFE target is not present in the thin film. The polymer after deposition loses structural order and becomes inevitably amorphous, which is expected in polymers sputtering due to the low mobility of the groups of atoms upon arrival at the substrate, preventing them to rearrange. The same observation, due to the same reasons, was observed for the PA deposited thin film.

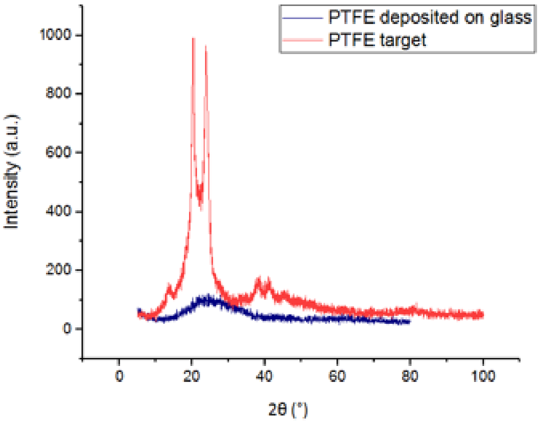

Figure 3.9: Diffractograms of the PTFE target and the PTFE thin film deposited onto glass. The same observation, due to the same reasons, was observed for the PA deposited thin film.

3.4 Chemical Characterization

The presence of characteristic chemical groups was evaluated by FTIR. This characterization has great interest in the context of polymers sputtering deposition because the resulting film may not be composed of the exact same material as the target, since new chemical bonds/functional groups can be formed by the atoms arriving at the substrate.

Only the films over silicon substrata were analyzed using the attenuated total reflection (ATR) sampling technique in order to prevent the presence of bands corresponding to the substrate material.

The FTIR spectrum of PTFE is relatively simple (Figure 3.10), due to its simple chemical structure – (-CF_2-)n. Comparing both spectra is possible to notice the presence of the same chemical bonds as the bands in the target profile also appear in the film profile, although less defined due to loss of crystallinity, as seen previously through X-ray diffraction. Furthermore, it is possible to see in the film profile the presence of chemical groups that were not constituents of the original polymer. This is the case of $-OH$ (3000-3200 cm^{-1}), $C = O$ and $-COOH$ in the region of 1600-1750 cm^{-1}.

The most intense bands are stretching vibrations of CF_2 and twisting of CF_2. The strong broad absorption band at 1230 cm^{-1} on the film spectrum represents an overlap of CF, CF_2 and CF_3 vibrations [95]. The band assignments of the absorption spectra for the PTFE target and the film resulting from its deposition are represented in Table 3.3.

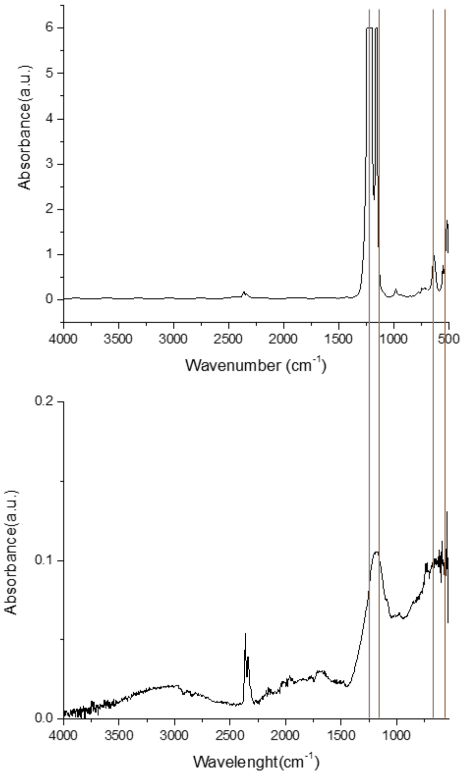

Figure 3.10: IR absorption spectrum of the PTFE target (upper figure) and the film resulting from its deposition on the silicon substrate (lower figure).

Table 3.3: Band assignments of the absorption spectra for the PTFE target and the film resulting from its deposition [96, 97].

IR bands (cm^{-1})	**Assignments**
1199	CF_2 symmetric stretching
1146	
640	CF deformation
630	
553	CF_2 bending
507	CF_2 twisting

The FTIR spectrum of PA is more complex due to the presence of more chemical groups (Figure 3.11). Both the target and thin film present bands in the same wavelengths indicating the presence of the same chemical bonds. The spectra differ only in two bands present in the film profile (at 1000 and 750 cm^{-1}), which represent SiO_2 from the substrate oxidation because the film is too thin. The band assignments of the absorption spectra for the PA target and the film resulting from its deposition are represented in Table 3.4.

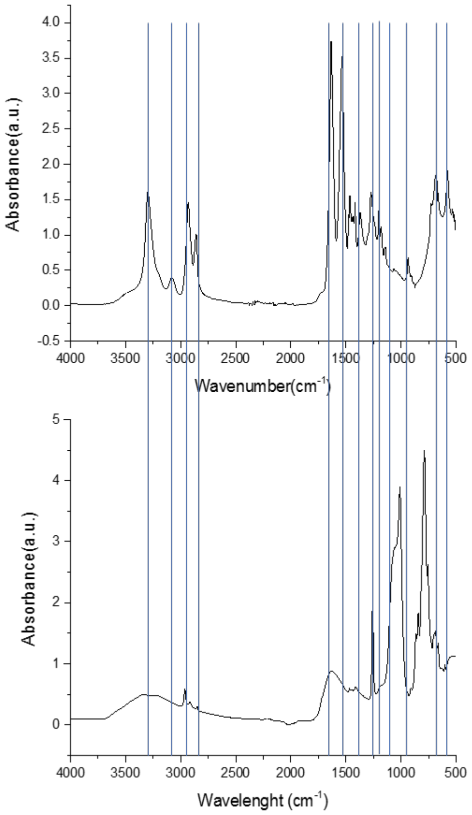

Figure 3.11: IR absorption spectrum of the PA target (upper figure) and the film resulting from its deposition on the silicon substrate (lower figure).

Table 3.4: Band assignments of the absorption spectra for the PA target and the film resulting from its deposition [98, 99].

IR bands (cm^{-1})	**Assignments**
3300	N-H stretch H-bonded
3070	N-H overtone
2930	Asymmetric CH_2 stretch
2860	Symmetric CH_2 stretch
1640	C=O stretch
1550	N-H bend
1478	CH_2 scissors
1373	
1200	CH_2 wagging
1180	
1136	C-C stretching
936	CO-NH in plane
684	C-C bending
578	C-C deformation

3.5 Wettability

Since this work highly focuses on the topography and chemistry of surfaces, it is very important to access the wettability as it is influenced by both the chemistry and the topography. Besides, the contact of a surface with water is obviously an essential factor to have into account when studying biomaterials, as they will experience direct contact with fluids.

The static contact angles of the thin films deposited onto glass and PDMS were measured with water and formamide. The results obtained are represented in the Table 3.5. The glass substrates samples were used to access only the influence of the chemical properties of the films, in opposition to the PDMS samples where both the chemistry and topography of the films can be responsible for the observed behavior.

Table 3.5: Static contact angles of the films deposited over glass and PDMS, measured with water or formamide.

Sample	**Contact angle (°)**	
	Water	Formamide
PTFE film on glass	107 ± 1	92 ± 2
PTFE film on PDMS	110 ± 3	-
PA film on glass	61 ± 4	32 ± 2
PA film on PDMS	81 ± 7	-

Firstly, it is important to notice than when biomaterials are considered, 65° is the limit angle between hydrophilic and hydrophobic surfaces [27]. Considering the contact angles for the PTFE film, it is clear the highly hydrophobic nature of this material. The chemical composition of this polymer, with many fluorocarbon groups, has great influence in its wettability since the angle measured for the glass substrata is already high when comparing with the PDMS substrata, which also considers topography. Considering the Cassie and Baxter model, the apparent contact angle increases when the contact area between asperities of the hydrophobic rough coating is reduced, which can be done increasing roughness [100]. This is in agreement with our results.

The results of the contact angle for the PA film on glass, values under 65°, indicate good liquid spreading on the surface, characteristic of hydrophilic materials. This was expected due to the presence of many polar groups in the film composition, namely $-COOH$ and $-NH_2$ as observed by FTIR analysis. The same film over PDMS presents a higher contact angle, being considered hydrophobic. This change in wettability is then related to an increase in roughness. However, the Wenzel theory indicates that with increasing surface roughness the apparent contact angle decreases for hydrophilic materials [100]. This seems to be in contradiction with the obtained results where the increase roughness of the thin film increases the contact angle. However, it must be considered that when roughness is induced to a surface, the liquid must overcome the barrier imposed by the topographic features. Since the PA has high affinity with water, over time the liquid kept spreading through the wrinkles, decreasing the contact angle until reaching a value of 59.3°, lower than the one measured in the glass substrata (Figure 3.12).

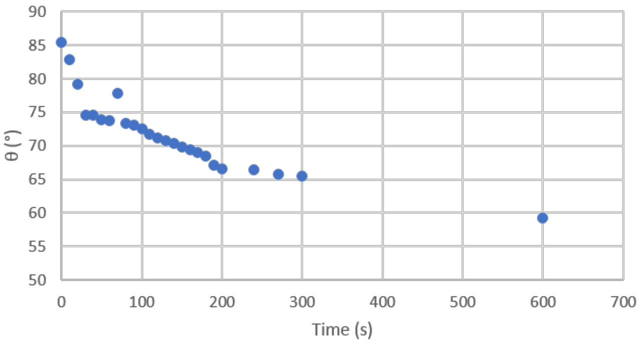

Figure 3.12: Contact angle variance with time for the PA film on PDMS.

3.6 Surface Energy

The surface energy was only determined for the glass substrate samples since the other surfaces presented a significant rough topography.

The equations 2.4 and 2.5, already mentioned in the previous chapter, allowed the determination of the surface tension of the surfaces, as well as its polar and dispersive components.

The values used for water were: γ_L=72.8 mJ/m^2; γ_L^d=21.8 mJ/m^2; γ_L^p=51 mJ/m^2. For formamide: γ_L=58.2 mJ/m^2; γ_L^d=39.5 mJ/m^2; γ_L^p=18.7 mJ/m^2.

Table 3.6: Surface tension of the films, as a sum of dispersive and polar components.

Thin film	γ_S (mJ/m^2)	γ_S^d (mJ/m^2)	γ_S^p (mJ/m^2)	γ_S^d (%)	γ_S^p (%)
PTFE	9.35	7.80	1.55	83.4	16.6
PA	49.94	37.07	12.87	74.2	25.8

Interactions caused by temporary fluctuations of the charge distribution in the atoms/molecules are called dispersive interactions (van der Waals interaction). Polar interactions comprise Coulomb interactions between permanent dipoles and between permanent and induced dipoles (e.g. hydrogen bonds).

The results presented in Table 3.6 show that the PTFE film presents a low surface tension with a very low polar component, characteristic of hydrophobic surfaces. However, this polar component is not as low as expected due to the presence of hydroxyl and carboxyl groups. The surface tension of the PA film presents a much higher value compared to the PTFE film, specially the polar component due to the presence of polar groups ($-COOH$, $-NH_2$). This results in a less stable, therefore, a more reactive surface, where stronger interactions are possible. A better adhesion is expected for this surface, which is in agreement with the contact angle measurements.

3.7 Zeta Potential

The zeta potential allows to evaluate the surface charge, and its magnitude gives an indication of the potential stability of the system. A value within the range of -30 to +30 mV indicates an unstable, reactive surface [101].

The zeta potentials of the films deposited over glass were measured and the results are as follows: -48.2 ± 5.4 mV for the PTFE film; -28.7 ± 0.9 mV for the PA film. Both films present negative zeta potentials, indicating the presence of negatively charged atoms/groups. These are due to the electronegativity of fluorine atoms, for the PTFE thin film. Also, $-CF_3$ groups have shown to increase the negative potential of the surface [102]. The value in the PA surface indicates that the ratio between $-COOH$ and $-NH_2$ groups is higher than 1. In fact, carbonyl and carboxylic groups are known to confer a negative charged surface, on the contrary of the $-NH_2$ that are responsible for positive values of zeta potential [103].

In terms of stability, the PTFE thin film is more stable, less reactive, than the PA surface. This is in agreement with the values of surface tensions, especially the contribution of polar and dispersive components. As discussed before these results are related with the type of chemical groups present in the surface of each thin film.

3.8 Mechanical Properties

It is important that biomaterials are both biological and mechanical compatible with the place of implantation. Since the human body is in constant motion, the implanted materials are subjected to different solicitation forces. Therefore, the knowledge beforehand of how the biomaterials behave during static and dynamic conditions is extremely important.

Nearly all biologic tissues exhibit viscoelastic behavior. The elastic deformation appears due to variations in the angle and bond distance between the atoms of the polymeric chain. Plastic deformation involves friction and breaking of a limited number of atomic bonds by the movement of dislocations [104]. This viscoelastic behavior is characterized by hysteresis in the response of the material to load or strain and is exhibited in many engineering materials such as the polymers PTFE, PA and PDMS [105]. Due to the viscoelastic behavior of polymers, careful design of mechanical tests is required since different parameters such as testing speeds may give different results.

Mechanical characterization of the PTFE and PA modified PDMS and the unmodified PDMS was done performing tensile, stress-relaxation and cyclic tests. During these tests was important to distinguish between longitudinal and transversal wrinkles to see if the wrinkles orientation had an influence on the mechanical properties of the material. The surface characterization of the samples following mechanical testing was also important to conclude how/if the surfaces topography changed in response to the mechanical forces applied.

3.8.1 Tensile Test

The samples were submitted to tensile tests, where a uniaxial force was applied straining them until rupture. The force and displacement values were normalized by the original specimen cross-sectional area (A_0) and length (l_0).

$$\varepsilon = \frac{l_i - l_0}{l_0} \tag{3.1}$$

$$\sigma = \frac{F}{A_0} \tag{3.2}$$

The obtained stress-strain curves are represented in Figure 3.13. The unmodified PDMS fractured at the highest strain value and presented the highest tensile strength compared to all the modified substrate. The PDMS with longitudinal PA wrinkles showed to be the less ductile, fracturing at the lowest strain.

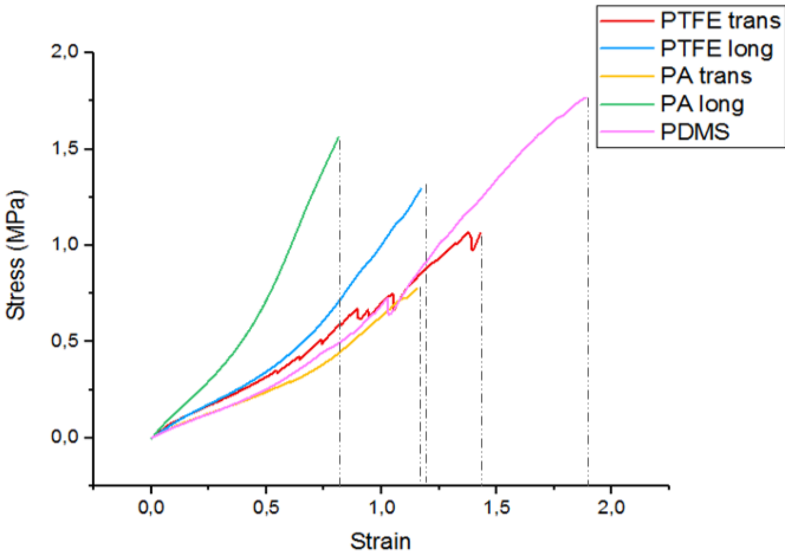

Figure 3.13: Stress-strain curves of the tensile tests performed for PTFE and PA modified PDMS and unmodified PDMS samples.

The elasticity modulus (E) is a measure of the stiffness of the material. It corresponds to the slope of the elastic region of the stress-strain curve, which respects Hooke's Law (equation 2.6) (it is the proportional coefficient). Since polymers have a viscoelastic behavior, the linear portion of the curve might not be easy to detect. Therefore, a tangent line was considered on the 1% strain point in order to determine the Young's modulus. Analyzing Table 3.7, we can conclude that, overall, the PDMS samples covered with thin films present higher E values than the unmodified substrate. The highest E value was registered for PDMS modified with the longitudinal wrinkles PA, while PDMS/PA with transversal wrinkles presented the lowest value.

The unmodified PDMS presented the highest value of toughness among all samples, meaning that was able to absorb the greatest amount of energy before fracturing. This value is given by the area under the stress-strain curve.

Although the thickness of the films is very small compared to the substrate, the mechanical properties of the modified PDMS are different from the original PDMS. These results were expected since the PTFE and PA films have different mechanical properties when compared with PDMS, this being the reason of wrinkling formation, as seen previously. Thus, the coating films have a composition that makes them stiffer than the PDMS substrate, due to the presence of unsaturated bonds and cross-linked chains.

Table 3.7: Young's modulus (E), toughness (U_t) and stress (σ_r) and strain (ε_r) at rupture, determined by tensile testing.

Polymer	**E (MPa)**	$\boldsymbol{U_t}$ **($\mathbf{10^6.}\boldsymbol{J.m^{-3}}$)**	$\boldsymbol{\sigma_r}$ **(MPa)**	$\boldsymbol{\varepsilon_r}$
PTFE trans	0.85	0.72	1.06	1.43
PTFE long	0.70	0.60	1.29	1.17
PA trans	0.54	0.37	0.78	1.15
PA long	1.24	0.51	1.56	0.81
PDMS	0.55	1.39	1.77	1.89

The mechanical properties of viscoelastic materials are extremely dependent on time. If a polymer sample is strained at low speed, its elastic modulus will be low, however, if strained at a higher speed, its elastic modulus will also increase [89]. Taking this into account, more tests should have been done with different strain rates in order to obtain more accurate results.

3.8.2 Relaxation Stress Test

When a polymeric sample is rapidly strained and kept under constant strain, the stress value needed to maintain this strain, decreases with time. This phenomenon is known as stress relaxation. These tests consisted in applying a strain rate of 7.5mm/min to all samples until reaching 27% of deformation and holding this strain for 2.5h. For each material, the test was repeated with three samples. The stress response with time for the PDMS samples coated with the longitudinal wrinkling PTFE thin films is represented in Figure 3.14. The results for all the other samples are represented in Figure A.1 of the Appendix.

The main goal of these tests was to evaluate the relaxation time constant, τ, for each sample. This constant is characteristic of each polymer at a certain temperature and quantifies its capacity to relax, to relieve the tension applied. [87, 88].The calculated values are summarized in Table 3.8. Since this test was performed within the elastic region of the materials, once a deformation is applied, the polymer is able to adapt reducing its stress response. The samples modified with the films present lower relaxation times, when compared with the unmodified PDMS, which indicates that they take less time to relieve the stress applied. This result is in agreement with the previous ones as the modified PDMS is less ductile than the unmodified substrate.

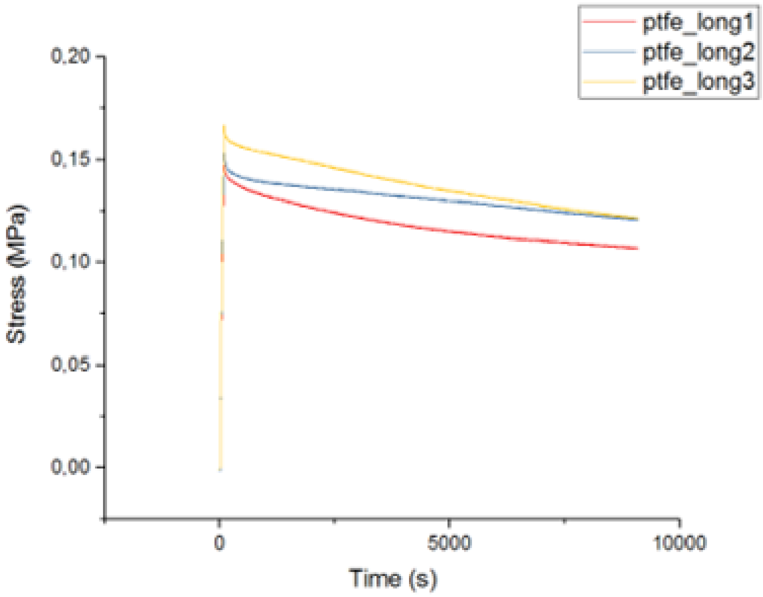

Figure 3.14: Variation of stress values with time for the PDMS/PTFE longitudinal wrinkles thin films, obtained from the stress relaxation test.

Table 3.8: Relaxation time (τ) of each tested sample and respective associated error.

Samples	$\tau \pm \delta\tau$ (h)
PTFE trans	4.3±0.9
PTFE long	8.8±1.4
PA trans	4.1±0.9
PA long	8.2±2.6
PDMS	14.1±3.9

3.8.3 Cyclic Tests

Fatigue is an important phenomenon in biomaterials, because the human body is constantly in motion both voluntary and involuntary, and both hard tissues and soft tissues are subjected to different repeated and cyclic mechanical solicitations. Therefore, cyclic tests were performed in all samples, repeating loading-unloading cycles. 10 cycles were made until reaching 20% of sample strain, at a strain rate of 7.5mm/min. A preload of 2N was applied to each specimen to ensure that all were strained at the same level at the beginning of the test.

The stress response of the specimen with the transversal PTFE wrinkles is represented in Figure 3.15b. It is possible to see in this figure that the unloading curve is different from the loading curve and, as the number of cycles increases, this difference decreases allowing the stress-strain curve to become more reproducible. This behavior was found for all samples tested (Figure 3.15a) and is a consequence of the viscoelastic behavior of the polymeric materials [89]. In fact, once a polymer is strained in the elastic region, even after the applied force is removed, a permanent deformation occurs. In fact, the polymer never resumes its initial dimensions. The scale of the deformation can be nano, micro or macro depending on the tested polymer and of the testing conditions. Nevertheless, each time a force is applied the permanent deformation will add and, consequently, the higher the number of solicitations the more differently the polymer will behave when compared with the untested material.

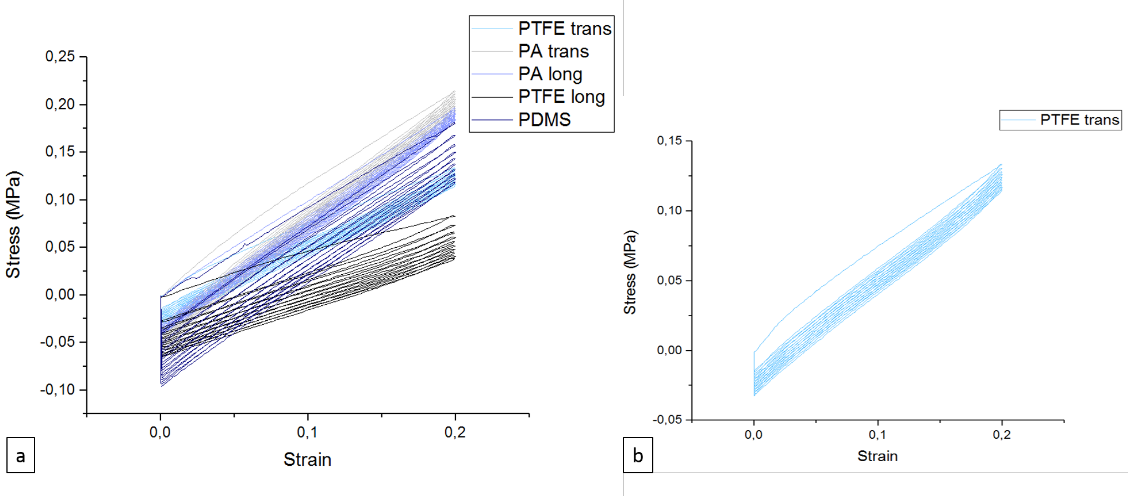

Figure 3.15: (a) Stress response with strain for all the samples. (b) Stress response for the PDMS sample with the PTFE film with transversal wrinkles.

The area enclosed by the loading and unloading paths is called the hysteresis loop and represents the energy dissipated as heat during the deformation and recovery phases. For a viscoelastic body, some of the strain energy is stored in the body as potential energy and some of it is dissipated as heat. Once the applied load is removed, the potential energy stored is available for the body to recover some of the deformation, however there is not enough energy for it to return to its original configuration [89, 106]. This way, the area of the hysteresis loop is an indicator of the permanent deformation suffered by the polymer. This area is also dependent upon the rate of strain employed to deform the body.

The hysteresis loop areas, for the 1st and 10th cycle of each sample, are shown in Table 3.9, where it is possible to confirm the decrease of the area with the number of cycles. The sample with the transversal PTFE wrinkles has the lowest amount of energy loss, suggesting that is the least plastic deformed.

Table 3.9: Areas of the hysteresis loop for the 1st and 10th cycle of each sample.

Samples	**Hysteresis loop area ($10^6.J.m^{-3}$)**	
	1st loop	10th loop
PTFE trans	2.98E-3	5.05E-4
PTFE long	3.85E-3	15.1E-4
PA trans	5.55E-3	12.1E-4
PA long	4.32E-3	3.25E-4
PDMS	3.73E-3	7.10E-4

3.8.4 Surface characterization after mechanical testing

The samples submitted to cyclic testing were characterized once again through IFM in order compare the topography with the samples prior to the tests. The micrographs obtained from this analysis can be seen in Figure 3.16.

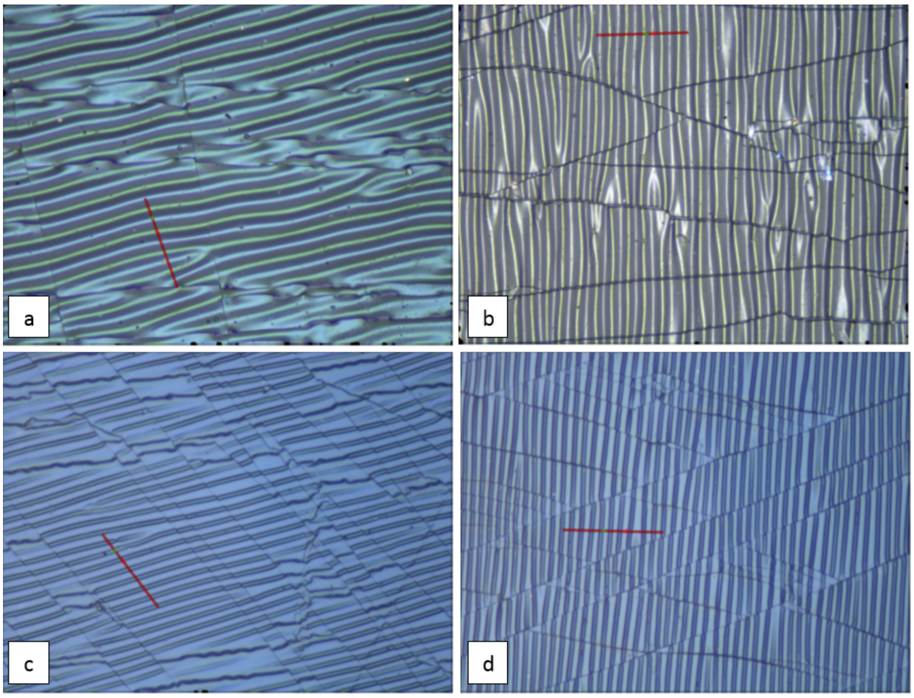

Figure 3.16: Optical micrographs from IFM analysis of the PTFE thin film with longitudinal (a) and transversal wrinkles (b) and the PA thin film with longitudinal (c) and transversal wrinkles (c). Red bars scale: (a) 60 μm; (b) 140 μm; (c) 30 μm; (d) 30 μm.

The micrographs show that the wrinkles are still present after the forces applied in the mechanical tests and their orientation remains the same. However, the substrates appear to be more damaged. The amplitude and wavelength of the wrinkles in the films, as well as the roughness parameters, are presented in Table 3.10. Once again, it is noticeable a great difference between the PTFE and PA wrinkles dimensions. It is interesting to notice that the kurtosis values, which in the previous analysis were all above 3 (Table 3.1) , have now decreased to values under 3 for both films with transversal wrinkles. This suggests that straining the samples in the wrinkles perpendicular direction induces a more flattened shape of the wrinkles. Therefore, it can be assumed that, to a certain point, the coating accompanied the substrate deformation, but as the coated PDMS is less ductile than the uncoated material, it plastic deforms creating the "fissures" observed in Figure 3.16.

Table 3.10: Amplitude and wavelength of the longitudinal and transversal wrinkles on the PTFE and PA films deposited on PDMS, after the mechanical testing, as well as roughness parameters determined through IFM analysis.

Film	$A \pm \delta A$ (μm)	$\lambda \pm \delta\lambda$ (μm)	Sa (μm)	Sq (μm)	Smax (μm)	Skew	Kurtosis
PTFE trans	2.9±0.5	28.0±0.8	1.14	1.38	7.46	-0.224	2.531
PTFE long	1.2±0.2	13.6±1.5	0.64	0.83	5.95	-0.199	3.805
PA trans	0.05±0.01	11.3±1.9	0.06	0.08	0.38	0.582	2.793
PA long	0.18±0.09	9.3±1.4	0.11	0.15	0.86	0.999	4.415

3.9 *In vitro* Tests

Stem cells (SCs) hold great promise for cell therapy, tissue engineering and regenerative medicine as well as pharmaceutical and biotechnological applications. They have the ability to self-renew and differentiate into specialized cell types depending upon their source of isolation. Mesenchymal stem cells (MSCs) can be isolated from adult sources such as bone marrow and adipose tissues or perinatal tissues, such as umbilical cord, cord blood, placenta and amniotic fluid. MSCs are multipotent and can differentiate into cell types such as osteogenic, chondrogenic, and adipogenic cells [107]. In comparison to adult MSCs, MSCs obtained from perinatal tissues exhibit higher growth and stemness potential [108]. Human Umbilical Cord Mesenchymal stem cells (hUC-MSCs) were the cells used in these tests. An integrated discussion will follow after the presentation of the obtained results.

3.9.1 Cell Viability

Cytocompatibilty studies of PDMS, PDMS/PT and PDMS/PA samples were assessed through the Presto Blue Viability assay at 24 hours, 72 hours, 120 hours and 168 hours. Results are expressed as mean and standard error of the mean (SD) and plotted over time (Figure 3.17) and statistical analysis is presented in Appendix (Figure A.2).

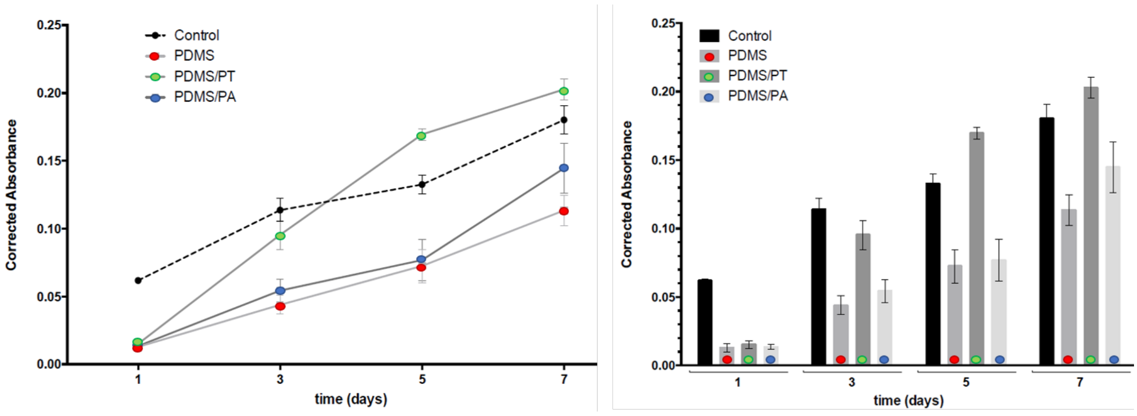

Figure 3.17: Corrected absorbance assessed by PrestoBlue® viability assay with hUC-MSCs, for up to 7 days (168 hours). Results presented as Mean ± SD.

Results show that after 24 hours incubation there is an inhibition of cell adhesion and initial proliferation in all the tested membranes. However, after 3 days of incubation PDMS/PT membranes show great increase in cell proliferation. This increase in PDMS/PT membranes remains until the end of the assay (7 days incubation), and is statistically different from the control tests. Nevertheless, PDMS/PT membranes show the highest cell viability rates between 3 days and 7 days. PDMS and PDMS/PA show similar cell viability profile through time, in terms of cell adhesion and proliferation, with significative difference from controls and PDMS/PT samples.

SEM was performed in all membranes (PDMS, PDMS/PT and PDMS/PA) and in glass coverslip seeded with hUC-MSCs. The samples preparation consists in chemical fixation of the cells with glutaraldehyde followed by a drying process to eliminate air and water from the biological samples. The dehydration process for all the membranes was only performed with ethanol series, since the chemical drying with HMDS created a reaction between the drying agent and the membranes, resulting in cracked like images (Figure 3.18).

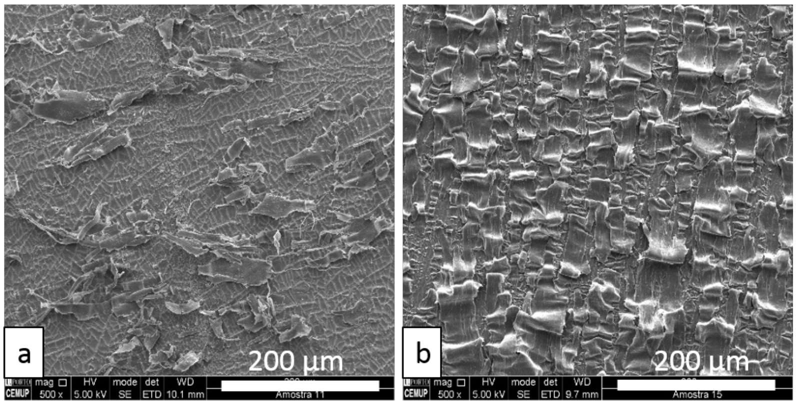

Figure 3.18: Scanning Electronic Microscopy (SEM) of (a) PDMS/PT membranes and (b) PDMS/PA membranes seeded with hUC-MSCs, following the sample preparation protocol including the chemical drying with HMDS.

Adhering cells were identified in all different groups (Figures 3.19, 3.20, 3.21, 3.22). The PDMS membranes (Figure 3.19) appear to be the ones with less adhering cells and weakest adhesion, compared to the others. Furthermore, they present a globular morphology, indicating that the cells are under stress or dead. Analyzing Figure 3.20, concerning the PDMS/PT membranes, is possible to see that the cells present good adhesion and spreading, exhibiting a normal star-like shape with a flat morphology. It is also interesting to notice that the cells seem to be aligned according to the wrinkles direction. However, the PDMS/PA membranes seem to present a larger quantity of adhering cells, homogeneously distributed, showing a more cohesive cell layer (Figure 3.21). Along with this, more cell-cell interactions are seen in this surface. A preferential direction of cell alignment and elongation is perceptible, showing again the influence of surface topography on cell behavior.

Figure 3.22 illustrates a glass coverslip sample with an intact cell layer adhered to its surface, which was used as a control.

EDS analysis was also performed in all samples (Figures 3.19, 3.20, 3.21). Differences were observed between groups, empathizing the different coating components. On the coated samples (Figures 3.20, 3.21), especially the PDMS/PA membrane, it was observed the detection of silica due to the films very low thickness.

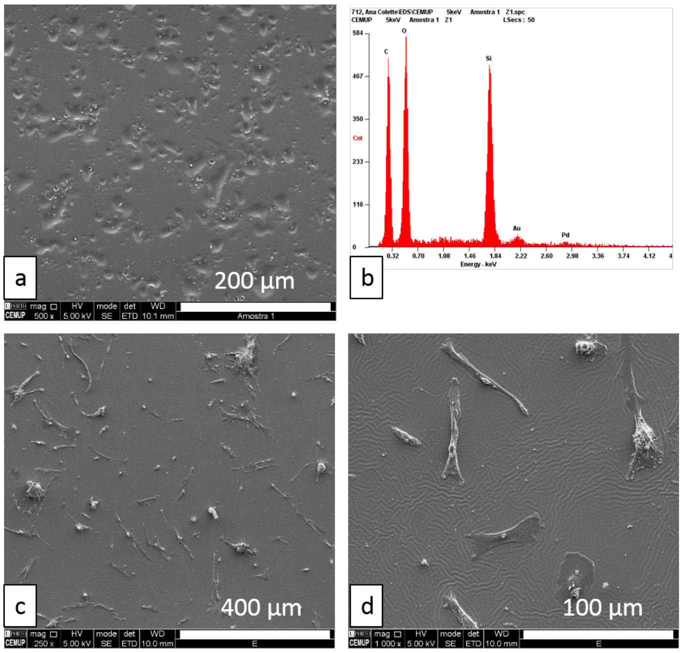
a
200 µm
b
C
O
Si
Au
Pd
Cnt
Energy - keV
c
400 µm
d
100 µm

Figure 3.19: Scanning Electronic Microscopy (SEM) of PDMS membranes. (a) shows PDMS membranes surface and (c, d) show PDMS membranes seeded with hUC-MSCs. EDS spectrum of the PDMS substrate.

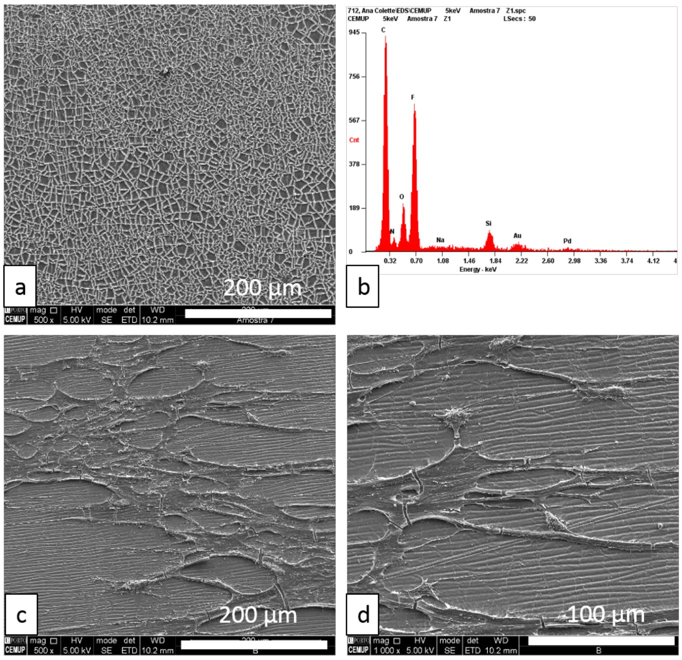
a
200 µm
b
C
F
O
N
Na
Si
Au
Pd
Cnt
Energy - keV
c
200 µm
d
100 µm

Figure 3.20: Scanning Electronic Microscopy (SEM) of PDMS/PT membranes. (a) shows PDMS/PT membranes surface and (c, d) show PDMS/PT membranes seeded with hUC-MSCs. EDS spectrum of the PDMS/PT substrate.

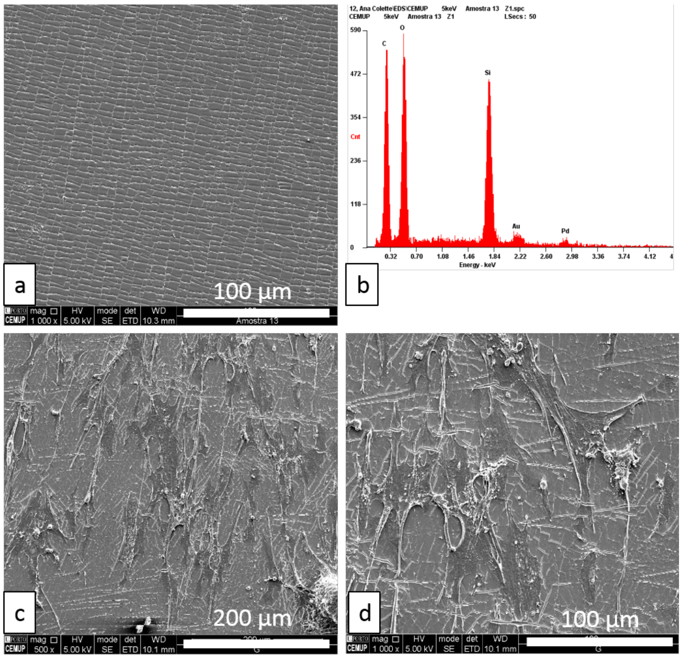

Figure 3.21: Scanning Electronic Microscopy (SEM) of PDMS/PA membranes. (a) shows PDMS/PA membranes surface and (c, d) show PDMS/PA membranes seeded with hUC-MSCs. EDS spectrum of the PDMS/PA substrate.

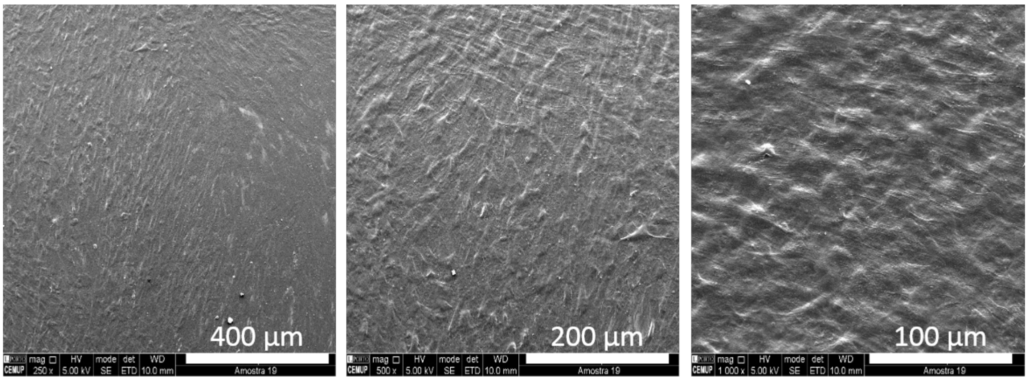

Figure 3.22: Scanning Electronic Microscopy (SEM) of glass coverslip seeded with hUC-MSCs.

3.9.2 Intracellular calcium

To correlate the MSCs ability to expand and survival capacity in the presence of the developed surfaces, the $[Ca^{2+}]$i of MSCs cultured in standard culture medium and in osteo-differentiation culture medium (Table 3.11) was determined by the epifluorescence technique using the Fura-2AM probe. The surfaces proved to be adequate to be used as scaffold associated with hUC-MSCs, since the $[Ca^{2+}]$i presented the normal intracellular concentration for viable mammals cells, after 10 days of in vitro culture in the presence of the PDMS, PDMS/PT and PDMS/PA ([109,110]), indicating that these cells presented normal morphology during expansion without a simultaneously increase of the [Ca^{2+}]i which leads to the onset cell death [111]. The MSCs cultured in osteogenic culture medium, presented higher concentration of [Ca^{2+}]i, due to the high concentration of Ca^{2+} in the culture medium, but still presenting cell viability.

Table 3.11: [Ca^{2+}]i measured by the epifluorescence technique, using the Fura-2- AM probe in non-differentiated hUC-MSCs cells, after 10 days of cell culture in presence of the PDMS, PDMS/PT and PDMS/PA membranes, and without biomaterial, the cells were kept in culture using standard culture medium or osteogenic medium. Results are presented as mean and standard error of the mean (SD).

Sample	**[Ca2+]i (nM)**	
	Standard culture medium	**Osteogenic culture medium**
PDMS	52.9±2.8	110.9±10.4
PDMS/PT	50.6±6.3	113.7±9.3
PDMS/PA	56.4±2.1	126.4±8.9
Cells	48.2±7.5	108.6±5.2

3.9.3 Osteogenic Differentiation: qualitative and semi--quantitative analysis

The PDMS, PDMS/PT and PDMS/PA membranes were evaluated as to their capacity to promote and/or inhibit osteogenic differentiation in hUCMSCs. They were incubated with hUC-MSCs and cultured in osteogenic culture medium for 21 days and Alizarin Red S Assay was used to assess osteogenic differentiation. Control samples were maintained in standard culture medium.

Control (cells only) show weaker ARS staining in standard medium conditions and strong staining in osteogenic supplemented conditions (Figure 3.23, Table 3.12). Statistical differences are detected in ARS staining when considering control and PDMS and PDMS/PT surfaces (Figure A.3 from the Appendix). Only PDMS/PA values are statistically similar to the ones of the controls.

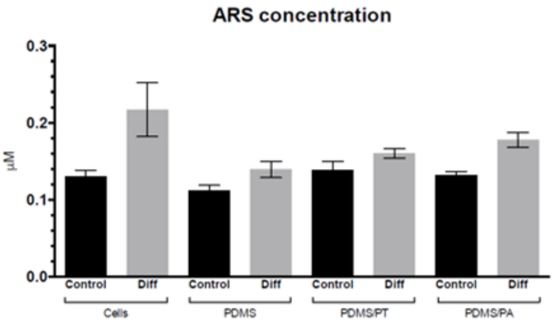

Figure 3.23: Osteogenic differentiation: Alizarin Red S concentration (μM) after 21 days. Control corresponds undifferentiated control and "Diff" to osteogenic differentiation culturing conditions. Results Presented as Mean ± SD.

Table 3.12: Quantification of osteogenic differentiation of hUC-MSCs seeded in PDMS, PDMS/PT and PDMS/PA membranes and cells alone, following Alizarin Red S staining protocol. Control: Undifferentiated control; Osteo Diff: Osteogenic Differentiation. Results Presented as Mean±SD.

Sample	**Alizarin Red S concentration (μM)**	
	Control	**Osteo Diff.**
Cells	13.03E-2±0.82E-2	21.70E-2±3.50E-2
PDMS	11.18E-2±0.71E-2	13.90E-2±1.05E-2
PDMS/PT	13.81E-2±1.14E-2	16.04E-2±0.61E-2
PDMS/PA	13.16E-2±0.50E-2	17.80E-2±0.96E-2

ARS staining shows that osteodifferentiation supplemented culture medium significantly increases cell differentiation in all samples tested. Although none of the surfaces prevents hUC-MSCs osteogenic differentiation, it seems that PDMS and PDMS/PT suppress its fully capacity for differentiation, unlike PDMS/PA that present similar results to the ones obtained for the controls. However, in standard culture medium conditions, PDMS/PT surfaces seem to induce osteogenic differentiation, showing the highest values of ARS staining among all samples, significantly different from PDMS substrate.

3.9.4 Discussion - *In vitro* tests

In this project, PDMS surfaces were modified through the deposition of thin films with nano- and microtopographical wrinkles. These surfaces were tested *in vitro* with the purpose of studying cell behavior in function of the chemical and physical properties of the substrates.

The cell viability study revealed that the PDMS/PT samples present the highest proliferation rate among all samples. This was unexpected due to the chemical properties of the PTFE film. It presents great hydrophobicity which is even more increased when roughness is also considered (Table 3.5). Besides, its composition containing many hydrophobic fluorocarbon groups ($-CF$, $-CF_2$, etc.) does not usually promote cell adhesion and proliferation (Figure 3.10). However, as observed in FTIR analysis, the PTFE film also incorporated other chemical groups such as $-OH$ and $-COOH$ which explain the positive results obtained for this surface. Furthermore, the double-rough topography (at nano and microscale) shows to positively influence cell behavior. In fact, the nanoroughness appears to play a major role in cell-material interaction because when considering the PA thin film, even dough having a favorable chemistry for cell adhesion and proliferation, does not have roughness at a nanolevel and presents worst results. At this length scale, the topography is able to affect sub-cellular behaviors, such as the organization and clustering of integrins. Tests with silicon/PT or glass/PT could have been done to confirm the topography influence in cell proliferation and adhesion.

From SEM analysis (Figures 3.19, 3.20, 3.21) it is possible to conclude that the PDMS/PT and PDMS/PA surfaces achieve better results than the PDMS substrate without any coating. The weak cell adhesion and proliferation in this sample was expected due to its hydrophobic nature. These findings suggest that thin wrinkling films are able to improve cell behavior on the substrate and that the sputtering method is a valid option for substrate treatment. Also, the topographic cues on the substrates were able to induce cell alignment, which has showed to play a role in tissue-biomaterial interface, affecting cell differentiation and functions [112, 113]. Furthermore, the decrease of ductility of the modified PDMS samples, compared to the unmodified PDMS, appears to be beneficial for cell behavior (Table 3.7).

The PDMS/PT samples, although with very low surface energy, specially the polar component, are able to support cell adhesion and spreading, as seen in the cell viability assay (Tables 3.6 and 3.5). In these images, the microscale wrinkles on this surface seem to positively influence cell behavior, namely cell alignment and spreading. The dimensions of the wrinkles compared to the cell size appear to be beneficial, as well as the “flattened” morphology of the wrinkles (Table 3.1).

Nevertheless, the PDMS/PA membranes seem to present the highest number of adhering cells and the presence of more cell-cell interactions is verified, which is essential for collective behavior (organization and alignment) as well as cell function and proliferation [114,115]. Cell adhesion and spreading are observed homogeneously throughout the surface. These positive results can be explained by the PA film chemical properties, since its hydrophilicity and presence of $-COOH$ and $-NH_2$ groups are likely to promote cell adhesion (Tables 3.5 and 3.4) [116]. A preferential direction of cell alignment and elongation is perceptible, which shows once more the influence of surface topography on cell behavior. However, these SEM images only characterize the surface morphology in a small area, which is only a qualitative assessment of the whole surface.

Following cell viability, cell differentiation was studied, more specifically cell osteodifferentiation. The intracellular calcium concentrations were accessed to ensure they were within the normal range during growth (normal culture medium) and differentiation (osteogenic medium). This was observed for all samples tested, which implies that successful cell growth and differentiation is possible. All samples tested presented similar osteogenic differentiation when normal culture medium was used. However, when cultured in osteogenic inducing medium, cells were not able to reach their maximum osteogenic differentiation potential, as seen for the control samples, the PDMS/PA samples being the ones with closer results to the control. It is clear that the physicochemical properties of the surfaces influence cell differentiation, namely the stiffness (E approximately 1 MPa) does not seem to induce cell osteodifferentiation. More studies should be done following other differentiation lineages and using different cell types.

Traditional 2D cell culture relies on flat surface adherence, typically on a Petri dish of glass or polystyrene, to provide mechanical support for cells. Cell growth in 2D monolayers allows the access to a similar amount of nutrients and growth factors present in the medium, which results in homogenous growth and proliferation [117]. This culture method has been used for SCs differentiation into many specialized cells, including chondrocytes, osteocytes, adipocytes, cardiomyocytes, smooth muscle cells and hepatocytes. However, it fails to accurately reproduce animal physiology and presents some drawbacks such as the lack of functional derivatives [108]. More recently, in an attempt of facing the problems of 2D culture, 3D culture methods have been developed to better mimic the composition and stiffness of the in vivo environment and improve physiological function, differentiation and drug responses [112].

PDMS has been extensively used to study stem cell physiology in the field of mechanobiology and microfluidic devices due to its transparency, low cost and ease of fabrication [108]. However, as seen previously, the PDMS chemistry makes it incompatible for cell adhesion and proliferation [118]. The results obtained for the *in vitro* tests validate the use of the PTFE and PA coated PDMS samples developed as cell substrates, since they support cell adhesion, proliferation and differentiation. Moreover, cell alignment was induced by the linear wrinkled topography of the films. These biomaterial surfaces can be applied for cell detection/screening, implantation, tissue engineering and biosensors.

Conclusions

On this project, PDMS substrates were surface modified through PTFE and PA sputtered coatings. These films were characterized and the presence of different chemical as well as physical properties, namely topography and stiffness, was verified. Furthermore, the effect of mechanically straining the samples on the wrinkled topography was accessed. In vitro studies were also performed to determine cell adhesion, proliferation and differentiation. The main conclusions obtained from this work are as follows:

- The sputtering method with PTFE and PA allows the formation of wrinkling topographies on PDMS substrates due to the temperature variations that both the film and the substrate, with different thermal expansion coefficients, are subjected;
- When PDMS substrate is strained prior to the deposition, the wrinkles created on the film present an aligned distribution, perpendicular to the direction of the applied force;
- The wrinkles size is dependent on the material used as target, as well as the conditions chosen for the sputtering process;
- The PTFE sputtering induces double scale (nano and micro) roughness;
- The PTFE-like film presents many fluorocarbon groups ($-CF$, $-CF_2$, ect.) and hydroxyl and carboxyl groups, has very low surface energy, being considered hydrophobic, opposite to the PA-like film composed of many carboxyl ($-COOH$) and some amine ($-NH_2$) groups (as the surface charge is negative);
- Both films present a negative zeta potential, indicating the presence of negatively charged atoms/groups;
- The thin PTFE and PA films affect the mechanical properties of the PDMS substrate;
- The elastic modulus is higher for the coated samples, compared to the PDMS alone, indicating that the material becomes less ductile upon film deposition.

- The PTFE and PA modified samples present lower relaxation times than the unmodified PDMS, meaning they take less time to relieve stress applied;
- The sample with the transversal PTFE wrinkles has the lowest amount of energy loss during deformation, suggesting that is the least plastic deformed;
- The surface wrinkles are maintained after samples being repeatedly strained;
- hUC-MSCs cultivated on PTFE and PA modified PDMS are able to adhere, proliferate and differentiate into osteogenic lineage;
- Surface nanoroughness appears to have a great influence in cell behavior;
- hUC-MSCs alignment is induced by the linear wrinkled topography of the films.

Future Work

The PDMS surface modified by sputtering results in a change of topography accompanied by a change of chemistry. Dependent on the target material used, the chemical properties of the surface can be manipulated, however the topography will too be modified. This way, the study of each factor alone, topography or chemistry, is difficult because, modifying one, will most likely also affect the other. The *in vitro* tests should be done for the same chemistry (same films) with no topography, using PTFE and PA glass modified, to conclude if the surface topography is responsible for the cellular behavior. Also, as nanoroughness appears to positively influence cell behavior, other materials with a more appealing chemistry could be used to create thin films with roughness at this length scale.

Cell alignment imposed by the topographic features of cell culture substrate is important for maintaining physiological phenotypes and functions, namely in anisotropic cardiac, neuronal and skeletal muscular tissues [112]. Different cell types, such as endothelial cells or neurons, could be used to further study the effect of the aligned wrinkly topography on cells orientation and differentiation. Also, the differentiation into other lineages other than osteogenic could be interesting as stiffness has showed to influence the differentiation faith.

Thin metal films, such as silver, could be deposited onto PDMS surfaces to make them electrical conductors, which has great interest in soft electronics. Also, the roughness conferred by sputtering could be beneficial for adhesion between the device materials.

Since the overall results achieved with the surfaces developed in this project were positive, it would be interesting to incorporate them in 3D cell culture methods, including microfluids and traction/compression forces, trying to further increase the similarities between this environment and the biological one and study cells response to these stimulus.

Bibliography

[1] Q. Zhou, P. T. Kühn, T. Huisman, E. Nieboer, C. Van Zwol, T. G. Van Kooten, and P. Van Rijn, "Directional nanotopographic gradients: a high-throughput screening platform for cell contact guidance," *Scientific reports*, vol. 5, p. 16240, 2015.

[2] A. Dolatshahi-Pirouz, T. Jensen, D. C. Kraft, M. Foss, P. Kingshott, J. L. Hansen, A. N. Larsen, J. Chevallier, and F. Besenbacher, "Fibronectin adsorption, cell adhesion, and proliferation on nanostructured tantalum surfaces," *Acs Nano*, vol. 4, no. 5, pp. 2874–2882, 2010.

[3] B. Ladoux and R.-M. Mège, "Mechanobiology of collective cell behaviours," *Nature Reviews Molecular Cell Biology*, vol. 18, no. 12, p. 743, 2017.

[4] A. W. Holle, J. L. Young, and J. P. Spatz, "In vitro cancer cell–ecm interactions inform in vivo cancer treatment," *Advanced drug delivery reviews*, vol. 97, pp. 270–279, 2016.

[5] J. Song, J. H. Shawky, Y. Kim, M. Hazar, P. R. LeDuc, M. Sitti, and L. A. Davidson, "Controlled surface topography regulates collective 3d migration by epithelial–mesenchymal composite embryonic tissues," *Biomaterials*, vol. 58, pp. 1–9, 2015.

[6] L. Bacakova, E. Filova, M. Parizek, T. Ruml, and V. Svorcik, "Modulation of cell adhesion, proliferation and differentiation on materials designed for body implants," *Biotechnology advances*, vol. 29, no. 6, pp. 739–767, 2011.

[7] D.-H. Kim, P. P. Provenzano, C. L. Smith, and A. Levchenko, "Matrix nanotopography as a regulator of cell function," *J Cell Biol*, vol. 197, no. 3, pp. 351–360, 2012.

[8] C. J. Flaim, D. Teng, S. Chien, and S. N. Bhatia, "Combinatorial signaling microenvironments for studying stem cell fate," *Stem cells and development*, vol. 17, no. 1, pp. 29–40, 2008.

[9] J. Rychly and B. J. Nebe, "Cell-material interaction," *BioNanoMaterials*, vol. 14, no. 3-4, pp. 153–160, 2013.

[10] J. Hayes, E. Czekanska, and R. Richards, "The cell–surface interaction," in *Tissue engineering III: cell-surface interactions for tissue culture*, pp. 1–31, Springer, 2011.

[11] A. Kapoor, E. H. Caporali, P. J. Kenis, and M. C. Stewart, "Microtopographically patterned surfaces promote the alignment of tenocytes and extracellular collagen," *Acta biomaterialia*, vol. 6, no. 7, pp. 2580–2589, 2010.

[12] C. J. Bettinger, R. Langer, and J. T. Borenstein, "Engineering substrate topography at the micro-and nanoscale to control cell function," *Angewandte Chemie International Edition*, vol. 48, no. 30, pp. 5406–5415, 2009.

[13] U. G. Wegst, H. Bai, E. Saiz, A. P. Tomsia, and R. O. Ritchie, "Bioinspired structural materials," *Nature materials*, vol. 14, no. 1, p. 23, 2015.

[14] Q. Zhou, J. Xie, M. Bao, H. Yuan, Z. Ye, X. Lou, and Y. Zhang, "Engineering aligned electrospun plla microfibers with nano-porous surface nanotopography for modulating the responses of vascular smooth muscle cells," *Journal of Materials Chemistry B*, vol. 3, no. 21, pp. 4439–4450, 2015.

[15] C. S. Davis and A. J. Crosby, "Mechanics of wrinkled surface adhesion," *Soft Matter*, vol. 7, no. 11, pp. 5373–5381, 2011.

[16] S. Kundu, C. S. Davis, T. Long, R. Sharma, and A. J. Crosby, "Adhesion of nonplanar wrinkled surfaces," *Journal of Polymer Science Part B: Polymer Physics*, vol. 49, no. 3, pp. 179–185, 2011.

[17] E. P. Chan, E. J. Smith, R. C. Hayward, and A. J. Crosby, "Surface wrinkles for smart adhesion," *Advanced Materials*, vol. 20, no. 4, pp. 711–716, 2008.

[18] A. I. Teixeira, G. A. Abrams, P. J. Bertics, C. J. Murphy, and P. F. Nealey, "Epithelial contact guidance on well-defined micro-and nanostructured substrates," *Journal of cell science*, vol. 116, no. 10, pp. 1881–1892, 2003.

[19] B. D. Ratner, A. S. Hoffman, F. J. Schoen, and J. E. Lemons, *Biomaterials science: an introduction to materials in medicine.* Elsevier, 2004.

[20] B. D. Boyan, T. W. Hummert, D. D. Dean, and Z. Schwartz, "Role of material surfaces in regulating bone and cartilage cell response," *Biomaterials*, vol. 17, no. 2, pp. 137–146, 1996.

[21] C. J. Wilson, R. E. Clegg, D. I. Leavesley, and M. J. Pearcy, "Mediation of biomaterial–cell interactions by adsorbed proteins: a review," *Tissue engineering*, vol. 11, no. 1-2, pp. 1–18, 2005.

[22] K. Anselme, "Osteoblast adhesion on biomaterials," *Biomaterials*, vol. 21, no. 7, pp. 667–681, 2000.

[23] C. Bökel and N. H. Brown, "Integrins in development: moving on, responding to, and sticking to the extracellular matrix," *Developmental cell*, vol. 3, no. 3,

pp. 311–321, 2002.

[24] E. Zamir and B. Geiger, “Molecular complexity and dynamics of cell-matrix adhesions,” *Journal of cell science*, vol. 114, no. 20, pp. 3583–3590, 2001.

[25] S. K. Mitra, D. A. Hanson, and D. D. Schlaepfer, “Focal adhesion kinase: in command and control of cell motility,” *Nature reviews Molecular cell biology*, vol. 6, no. 1, p. 56, 2005.

[26] P. Roach, D. Farrar, and C. C. Perry, “Interpretation of protein adsorption: surface-induced conformational changes,” *Journal of the American Chemical Society*, vol. 127, no. 22, pp. 8168–8173, 2005.

[27] E. A. Vogler, “Structure and reactivity of water at biomaterial surfaces,” *Advances in colloid and interface science*, vol. 74, no. 1-3, pp. 69–117, 1998.

[28] S. Ferreira, “*Wrinkled surfaces: serão as rugas a melhor superfície*,” Master’s thesis, *Universidade de Coimbra*, 2017.

[29] L. Tang, P. Thevenot, and W. Hu, “Surface chemistry influences implant biocompatibility,” *Current topics in medicinal chemistry*, vol. 8, no. 4, pp. 270–280, 2008.

[30] D. R. Schmidt, H. Waldeck, and W. J. Kao, “Protein adsorption to biomaterials,” in *Biological interactions on materials surfaces*, pp. 1–18, Springer, 2009.

[31] B. K. Mann, A. S. Gobin, A. T. Tsai, R. H. Schmedlen, and J. L. West, “Smooth muscle cell growth in photopolymerized hydrogels with cell adhesive and proteolytically degradable domains: synthetic ecm analogs for tissue engineering,” *Biomaterials*, vol. 22, no. 22, pp. 3045–3051, 2001.

[32] K. S. Masters and K. S. Anseth, “Cell–material interactions,” *Advances in Chemical Engineering*, vol. 29, pp. 7–46, 2004.

[33] H.-I. Chang and Y. Wang, “Cell responses to surface and architecture of tissue engineering scaffolds,” in *Regenerative medicine and tissue engineering-cells and biomaterials*, InTech, 2011.

[34] M. Nikkhah, F. Edalat, S. Manoucheri, and A. Khademhosseini, “Engineering microscale topographies to control the cell–substrate interface,” *Biomaterials*, vol. 33, no. 21, pp. 5230–5246, 2012.

[35] P. Slepicka, N. S. Kasalkova, J. Siegel, Z. Kolska, L. Bacakova, and V. Svorcik, “Nano-structured and functionalized surfaces for cytocompatibility improvement and bactericidal action,” *Biotechnology advances*, vol. 33, no. 6, pp. 1120–1129, 2015.

[36] G. Abagnale, M. Steger, V. H. Nguyen, N. Hersch, A. Sechi, S. Joussen, B. Denecke, R. Merkel, B. Hoffmann, A. Dreser, *et al.*, “Surface topogra-

phy enhances differentiation of mesenchymal stem cells towards osteogenic and adipogenic lineages," *Biomaterials*, vol. 61, pp. 316–326, 2015.

[37] M. Arnold, V. C. Hirschfeld-Warneken, T. Lohmuller, P. Heil, J. Blummel, E. A. Cavalcanti-Adam, M. López-García, P. Walther, H. Kessler, B. Geiger, *et al.*, "Induction of cell polarization and migration by a gradient of nanoscale variations in adhesive ligand spacing," *Nano letters*, vol. 8, no. 7, pp. 2063–2069, 2008.

[38] A. T. Nguyen, S. R. Sathe, and E. K. Yim, "From nano to micro: topographical scale and its impact on cell adhesion, morphology and contact guidance," *Journal of Physics: Condensed Matter*, vol. 28, no. 18, p. 183001, 2016.

[39] R. V. Goreham, A. Mierczynska, L. E. Smith, R. Sedev, and K. Vasilev, "Small surface nanotopography encourages fibroblast and osteoblast cell adhesion," *Rsc Advances*, vol. 3, no. 26, pp. 10309–10317, 2013.

[40] X. Yao, R. Peng, and J. Ding, "Cell–material interactions revealed via material techniques of surface patterning," *Advanced materials*, vol. 25, no. 37, pp. 5257–5286, 2013.

[41] A. Wood, "Contact guidance on microfabricated substrata: the response of teleost fin mesenchyme cells to repeating topographical patterns," *Journal of cell science*, vol. 90, no. 4, pp. 667–681, 1988.

[42] P. Clark, P. Connolly, A. Curtis, J. Dow, and C. Wilkinson, "Cell guidance by ultrafine topography in vitro," *Journal of cell science*, vol. 99, no. 1, pp. 73–77, 1991.

[43] A. Webb, P. Clark, J. Skepper, A. Compston, and A. Wood, "Guidance of oligodendrocytes and their progenitors by substratum topography," *Journal of cell science*, vol. 108, no. 8, pp. 2747–2760, 1995.

[44] C. J. Bettinger, Z. Zhang, S. Gerecht, J. T. Borenstein, and R. Langer, "Enhancement of in vitro capillary tube formation by substrate nanotopography," *Advanced materials*, vol. 20, no. 1, pp. 99–103, 2008.

[45] E. Den Braber, J. De Ruijter, L. Ginsel, A. Von Recum, and J. Jansen, "Orientation of ecm protein deposition, fibroblast cytoskeleton, and attachment complex components on silicone microgrooved surfaces," *Journal of Biomedical Materials Research: An Official Journal of The Society for Biomaterials, The Japanese Society for Biomaterials, and the Australian Society for Biomaterials*, vol. 40, no. 2, pp. 291–300, 1998.

[46] P. Uttayarat, G. K. Toworfe, F. Dietrich, P. I. Lelkes, and R. J. Composto, "Topographic guidance of endothelial cells on silicone surfaces with micro-to nanogrooves: Orientation of actin filaments and focal adhesions," *Journal of*

Biomedical Materials Research Part A: An Official Journal of The Society for Biomaterials, The Japanese Society for Biomaterials, and The Australian Society for Biomaterials and the Korean Society for Biomaterials, vol. 75, no. 3, pp. 668–680, 2005.

[47] Y. Li, G. Huang, X. Zhang, L. Wang, Y. Du, T. J. Lu, and F. Xu, “Engineering cell alignment in vitro,” *Biotechnology advances*, vol. 32, no. 2, pp. 347–365, 2014.

[48] S. Kidambi, N. Udpa, S. A. Schroeder, R. Findlan, I. Lee, and C. Chan, “Cell adhesion on polyelectrolyte multilayer coated polydimethylsiloxane surfaces with varying topographies,” *Tissue engineering*, vol. 13, no. 8, pp. 2105–2117, 2007.

[49] Q. Zhou, O. Castaneda Ocampo, C. F. Guimaraes, P. T. Kühn, T. G. van Kooten, and P. van Rijn, “Screening platform for cell contact guidance based on inorganic biomaterial micro/nanotopographical gradients,” *ACS applied materials & interfaces*, vol. 9, no. 37, pp. 31433–31445, 2017.

[50] Q. Zhou, P. Wünnemann, P. T. Kühn, J. de Vries, M. Helmin, A. Böker, T. G. van Kooten, and P. van Rijn, “Mechanical properties of aligned nanotopologies for directing cellular behavior,” *Advanced Materials Interfaces*, vol. 3, no. 18, p. 1600275, 2016.

[51] F. Greco, T. Fujie, L. Ricotti, S. Taccola, B. Mazzolai, and V. Mattoli, “Microwrinkled conducting polymer interface for anisotropic multicellular alignment,” *ACS applied materials & interfaces*, vol. 5, no. 3, pp. 573–584, 2013.

[52] A. Engler, L. Bacakova, C. Newman, A. Hategan, M. Griffin, and D. Discher, “Substrate compliance versus ligand density in cell on gel responses,” *Biophysical journal*, vol. 86, no. 1, pp. 617–628, 2004.

[53] A. J. Engler, S. Sen, H. L. Sweeney, and D. E. Discher, “Matrix elasticity directs stem cell lineage specification,” *Cell*, vol. 126, no. 4, pp. 677–689, 2006.

[54] R. J. McMurray, N. Gadegaard, P. M. Tsimbouri, K. V. Burgess, L. E. McNamara, R. Tare, K. Murawski, E. Kingham, R. O. Oreffo, and M. J. Dalby, “Nanoscale surfaces for the long-term maintenance of mesenchymal stem cell phenotype and multipotency,” *Nature materials*, vol. 10, no. 8, p. 637, 2011.

[55] J. Fiedler, B. Özdemir, J. Bartholomä, A. Plettl, R. E. Brenner, and P. Ziemann, “The effect of substrate surface nanotopography on the behavior of multipotnent mesenchymal stromal cells and osteoblasts,” *Biomaterials*, vol. 34, no. 35, pp. 8851–8859, 2013.

[56] T. J. Webster, C. Ergun, R. H. Doremus, R. W. Siegel, and R. Bizios, “En-

hanced functions of osteoblasts on nanophase ceramics," *Biomaterials*, vol. 21, no. 17, pp. 1803–1810, 2000.

[57] J. Rodríguez-Hernández, "Wrinkled interfaces: Taking advantage of surface instabilities to pattern polymer surfaces," *Progress in Polymer Science*, vol. 42, pp. 1–41, 2015.

[58] E. Daramola, "Fabrication of micro/nano-structured wrinkles through surface modifcation of poly(dimethylsiloxane)."

[59] T. Ohzono and M. Shimomura, "Ordering of microwrinkle patterns by compressive strain," *Physical Review B*, vol. 69, no. 13, p. 132202, 2004.

[60] "Sputtering." [Accessed online Jun 2018] $http : //users.wfu.edu/ucerkb/Nan242/L07 - Sputtering_a.pdf$.

[61] R. Wördenweber, "Deposition technologies, growth and properties of high-t c films," in *High-Temperature Superconductors*, pp. 3–38e, Elsevier, 2011.

[62] J. A. Rogers, R. Ghaffari, and D.-H. Kim, *Stretchable Bioelectronics for Medical Devices and Systems.* Springer, 2016.

[63] V. F. Sciuti, C. C. Melo, L. B. Canto, and R. B. Canto, "Influence of surface crystalline structures on dsc analysis of ptfe," *Materials Research*, vol. 20, no. 5, pp. 1350–1359, 2017.

[64] "Polytetrafluoroethylene." [Accessed online Jul 2018] http://www.goodfellow.com/E/Polytetrafluoroethylene-Polymer.html.

[65] "Polyamides (nylons)." [Accessed online Jul 2018] http://www.steinwall.com/wp-content/uploads/2016/05/Nylon.pdf.

[66] "Infinitefocus. alicona." [Accessed online Jul 2018] https://www.alicona.com/products/infinitefocus/.

[67] "What is an infinite focus microscope." [Accessed online Jul 2018] https://www.shu.ac.uk/research/specialisms/materials-and-engineering-research-institute/facilities/infinite-focus-microscope.

[68] "Atomic force microscopy." [Accessed online Jul 2018] https://www.nanoscience.com/technology/afm-technology/.

[69] "Afm: Dynamic modes." [Accessed online Jul 2018].

[70] "The atomic force microscope (afm)." [Accessed online Jul 2018] https://www.microscopemaster.com/atomic-force-microscope.html.

[71] "Scanning electron microscopy (sem)." [Accessed online Jul 2018] $https : //serc.carleton.edu/research_education/geochemsheets/techniques/SEM.html$.

[72] "How an sem works." [Accessed online Jul 2018] https://www.nanoscience.com/technology/sem-technology/how-sem-works/.

[73] “X-ray diffraction.” [Accessed online Jul 2018] *https : //www.rigaku.com/en/techniques/xrd.*

[74] “X-ray powder diffraction (xrd).” [Accessed online Jul 2018] *https : //serc.carleton.edu/research*$_e$*ducation/geochemsheets/techniques/XRD.html.*

[75] “Fourier transform infrared spectroscopy.” [Accessed online Jul 2018] https://www.mee-inc.com/hamm/fourier-transform-infrared-spectroscopy-ftir/.

[76] “Ftir basics.” [Accessed online Jul 2018] https://www.thermofisher.com/pt/en/home/industrial/spectroscopy-elemental-isotope-analysis/spectroscopy-elemental-isotope-analysis-learning-center/molecular-spectroscopy-information/ftir-information/ftir-basics.html.

[77] W. A. Zisman, “Relation of the equilibrium contact angle to liquid and solid constitution.,” *Advan. Chem. Ser.*, vol. 43, pp. 1–51, 1964.

[78] R. J. Good, “Contact angle, wetting, and adhesion: a critical review,” *Journal of adhesion science and technology*, vol. 6, no. 12, pp. 1269–1302, 1992.

[79] “Initiation to contact angle.” [Accessed online Jul 2018] http://www.cscscientific.com/csc-cientific-blog/initiation-to-contact-angle.

[80] K. Kubiak, M. Wilson, T. Mathia, and P. Carval, “Wettability versus roughness of engineering surfaces,” *Wear*, vol. 271, no. 3-4, pp. 523–528, 2011.

[81] I. Milne, R. O. Ritchie, and B. L. Karihaloo, *Comprehensive structural integrity: Cyclic loading and fatigue*, vol. 4. Elsevier, 2003.

[82] D. K. Owens and R. Wendt, “Estimation of the surface free energy of polymers,” *Journal of applied polymer science*, vol. 13, no. 8, pp. 1741–1747, 1969.

[83] S. Bhattacharjee, “Dls and zeta potential–what they are and what they are not?,” *Journal of Controlled Release*, vol. 235, pp. 337–351, 2016.

[84] A. Carré and K. L. Mittal, *Surface and interfacial aspects of cell adhesion.* CRC Press, 2011.

[85] “Viscoelasticity and master curves.” [Accessed online Jul 2018] http://www.open.edu/openlearn/science-maths-technology/science/chemistry/introduction-polymers/content-section-5.3.

[86] “Tensile testing.” [Accessed online Jul 2018] http://www.instron.us/en-us/our-company/library/test-types/tensile-test.

[87] D. Roylance, “Engineering viscoelasticity.” [Accessed online Jul 2018] http://web.mit.edu/course/3/3.11/www/modules/visco.pdf.

[88] R. K. Roeder, “Mechanical characterization of biomaterials,” in *Characterization of biomaterials*, pp. 49–104, Elsevier, 2013.

[89] “The response of viscoelastic materials.” [Accessed online Jul 2018] $http://homepages.engineering.auckland.ac.nz/\ pkel015/SolidMechanicsBooks/Part_I/BookSM_Part_I/10_Viscoelasticity/10_Viscoelasticity_01_Intro.pdf$.

[90] S. K. Fisher, L. M. Domask, and R. M. Roland, “Muscarinic receptor regulation of cytoplasmic ca2+ concentrations in human sk-n-sh neuroblastoma cells: Ca2+ requirements for phospholipase c activation.,” *Molecular pharmacology*, vol. 35, no. 2, pp. 195–204, 1989.

[91] G. Grynkiewicz, M. Poenie, and R. Y. Tsien, “A new generation of ca2+ indicators with greatly improved fluorescence properties.,” *Journal of Biological Chemistry*, vol. 260, no. 6, pp. 3440–3450, 1985.

[92] C. A. Gregory, W. G. Gunn, A. Peister, and D. J. Prockop, “An alizarin red-based assay of mineralization by adherent cells in culture: comparison with cetylpyridinium chloride extraction,” *Analytical biochemistry*, vol. 329, no. 1, pp. 77–84, 2004.

[93] E. Gadelmawla, M. Koura, T. Maksoud, I. Elewa, and H. Soliman, “Roughness parameters,” *Journal of Materials Processing Technology*, vol. 123, no. 1, pp. 133–145, 2002.

[94] H. Biederman, “Rf sputtering of polymers and its potential application,” *Vacuum*, vol. 59, no. 2-3, pp. 594–599, 2000.

[95] Y. Zhang, G. Yang, E. Kang, K. Neoh, W. Huang, A. Huan, and D. Lai, “Characterization of fluoropolymer films deposited by magnetron sputtering of poly (tetrafluoroethylene) and plasma polymerization of heptadecafluoro-1-decene (hdfd) on (100)-oriented single-crystal silicon substrates,” *Surface and Interface Analysis: An International Journal devoted to the development and application of techniques for the analysis of surfaces, interfaces and thin films*, vol. 34, no. 1, pp. 10–18, 2002.

[96] D. D. Fazullin, G. V. Mavrin, M. P. Sokolov, and I. G. Shaikhiev, “Infrared spectroscopic studies of the ptfe and nylon membranes modified polyaniline,” *Modern Applied Science*, vol. 9, no. 1, p. 242, 2014.

[97] J. Mihály, S. Sterkel, H. M. Ortner, L. Kocsis, L. Hajba, É. Furdyga, and J. Mink, “Ftir and ft-raman spectroscopic study on polymer based high pressure digestion vessels,” *Croatica chemica acta*, vol. 79, no. 3, pp. 497–501, 2006.

[98] N. Vasanthan, “Crystallinity determination of nylon 66 by density measurement and fourier transform infrared (ftir) spectroscopy,” *Journal of Chemical Education*, vol. 89, no. 3, pp. 387–390, 2012.

[99] J. Charles, G. Ramkumaar, S. Azhagiri, and S. Gunasekaran, “Ftir and ther-

mal studies on nylon-66 and 30% glass fibre reinforced nylon-66," *Journal of Chemistry*, vol. 6, no. 1, pp. 23–33, 2009.

[100] S. Veeramasuneni, J. Drelich, J. Miller, and G. Yamauchi, "Hydrophobicity of ion-plated ptfe coatings," *Progress in Organic Coatings*, vol. 31, no. 3, pp. 265–270, 1997.

[101] "Zeta potential for measurement of stability of nanoparticles." [Accessed online Jul 2018] http://www.pharmainfo.net/book/emerging-trends-nanotechnology-pharmacy-physicochemical-characterization-nanoparticles/zeta.

[102] G. Altankov, K. Richau, and T. Groth, "The role of surface zeta potential and substratum chemistry for regulation of dermal fibroblasts interaction," *Materialwissenschaft und Werkstofftechnik: Entwicklung, Fertigung, Prüfung, Eigenschaften und Anwendungen technischer Werkstoffe*, vol. 34, no. 12, pp. 1120–1128, 2003.

[103] I. Carvalho, M. Henriques, J. C. Oliveira, C. F. A. Alves, A. P. Piedade, and S. Carvalho, "Influence of surface features on the adhesion of staphylococcus epidermidis to ag–ticn thin films," *Science and technology of advanced materials*, vol. 14, no. 3, p. 035009, 2013.

[104] "Chapter 16. polymers. characteristics, applications and processing. stress-strain behavior." [Accessed online Jul 2018] http://www.virginia.edu/bohr/mse209/chapter16.htm.

[105] J. D. Berg, "Mechanical testing device for viscoelastic biomaterials," 2010.

[106] N. Özkaya, D. Leger, D. Goldsheyder, and M. Nordin, *Fundamentals of biomechanics: equilibrium, motion, and deformation.* Springer, 2016.

[107] M. F. Pittenger, A. M. Mackay, S. C. Beck, R. K. Jaiswal, R. Douglas, J. D. Mosca, M. A. Moorman, D. W. Simonetti, S. Craig, and D. R. Marshak, "Multilineage potential of adult human mesenchymal stem cells," *science*, vol. 284, no. 5411, pp. 143–147, 1999.

[108] C. McKee and G. R. Chaudhry, "Advances and challenges in stem cell culture," *Colloids and Surfaces B: Biointerfaces*, vol. 159, pp. 62–77, 2017.

[109] D. E. Clapham, "Calcium signaling," *Cell*, vol. 131, no. 6, pp. 1047–1058, 2007.

[110] A. Tay, "Tools to measure change in intracellular calcium levels." [Accessed online Aug 2018] https://blog.quartzy.com/2017/05/19/tools-measure-change-intracellular-calcium-levels.

[111] M. Martínez, N. A. Martínez, and W. I. Silva, "Measurement of the intracellular calcium concentration with fura-2 am using a fluorescence plate reader,"

2017.

[112] C. G. Anene-Nzelu, K. Y. Peh, A. Fraiszudeen, Y. H. Kuan, S. H. Ng, Y. C. Toh, H. L. Leo, and H. Yu, "Scalable alignment of three-dimensional cellular constructs in a microfluidic chip," *Lab on a Chip*, vol. 13, no. 20, pp. 4124–4133, 2013.

[113] D. W. Hamilton, S. Ghrebi, H. Kim, B. Chehroudi, and D. M. Brunette, "Surface topography and cell behaviour," *Encyclopedia of biomaterials and biomedical engineering. New York: Taylor and Francis*, pp. 1–15, 2006.

[114] Q. Wei and H. Huang, "Insights into the role of cell–cell junctions in physiology and disease," in *International review of cell and molecular biology*, vol. 306, pp. 187–221, Elsevier, 2013.

[115] G. M. Cooper and D. Ganem, "The cell: a molecular approach," *Nature Medicine*, vol. 3, no. 9, pp. 1042–1042, 1997.

[116] D. Bhattacharyya, H. Xu, R. R. Deshmukh, R. B. Timmons, and K. T. Nguyen, "Surface chemistry and polymer film thickness effects on endothelial cell adhesion and proliferation," *Journal of Biomedical Materials Research Part A*, vol. 94, no. 2, pp. 640–648, 2010.

[117] K. Duval, H. Grover, L.-H. Han, Y. Mou, A. F. Pegoraro, J. Fredberg, and Z. Chen, "Modeling physiological events in 2d vs. 3d cell culture," *Physiology*, vol. 32, no. 4, pp. 266–277, 2017.

[118] S. Halldorsson, E. Lucumi, R. Gómez-Sjöberg, and R. M. Fleming, "Advantages and challenges of microfluidic cell culture in polydimethylsiloxane devices," *Biosensors and Bioelectronics*, vol. 63, pp. 218–231, 2015.

Appendices

A

Appendix

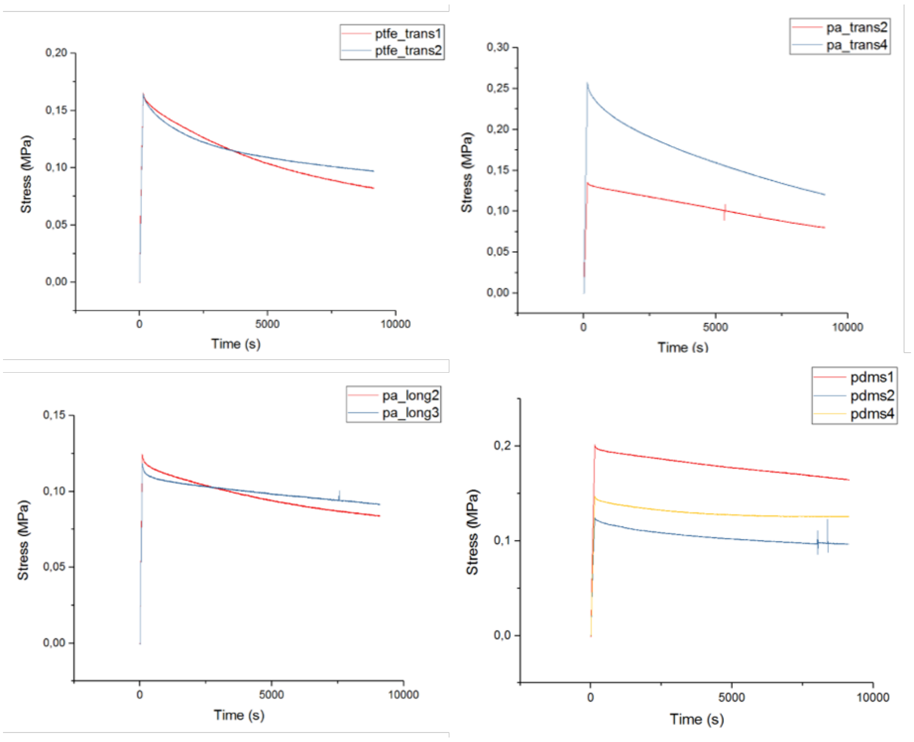

Figure A.1: Stress variance with time for all the samples. Results obtained from the stress relaxation tests.

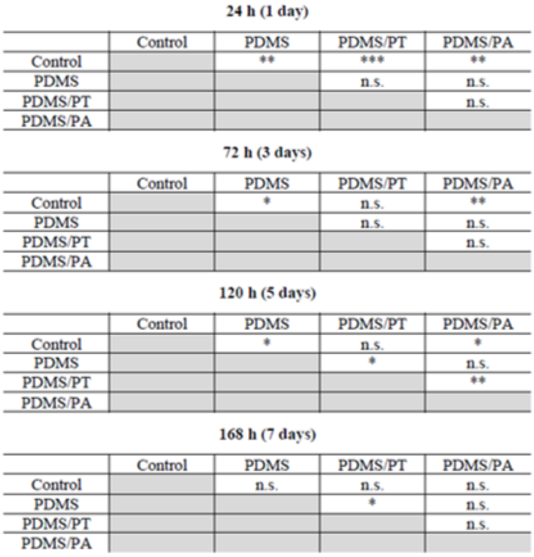

24 h (1 day)

	Control	PDMS	PDMS/PT	PDMS/PA
Control		**	***	**
PDMS			n.s.	n.s.
PDMS/PT				n.s.
PDMS/PA				

72 h (3 days)

	Control	PDMS	PDMS/PT	PDMS/PA
Control		*	n.s.	**
PDMS			n.s.	n.s.
PDMS/PT				n.s.
PDMS/PA				

120 h (5 days)

	Control	PDMS	PDMS/PT	PDMS/PA
Control		*	n.s.	*
PDMS			*	n.s.
PDMS/PT				**
PDMS/PA				

168 h (7 days)

	Control	PDMS	PDMS/PT	PDMS/PA
Control		n.s.	n.s.	n.s.
PDMS			*	n.s.
PDMS/PT				n.s.
PDMS/PA				

Figure A.2: Statistical analysis of Presto Blue Viability assay of hUC-MSCs seeded scaffolds. Significance of the results is indicated according to P values with one, two, three or four of the symbols (*) corresponding to $0.01 \leq P < 0.05$; $0.001 \leq P < 0.01$; $0.0001 \leq P < 0.001$ and $P < 0.0001$, respectively; ns, not significant.

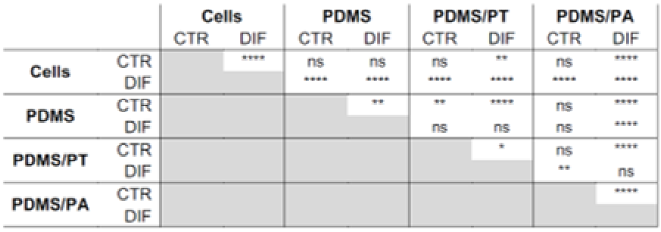

		Cells		PDMS		PDMS/PT		PDMS/PA	
		CTR	DIF	CTR	DIF	CTR	DIF	CTR	DIF
Cells	CTR		****	ns	ns	ns	**	ns	****
	DIF			****	****	****	****	****	****
PDMS	CTR				**	**	****	ns	****
	DIF					ns	ns	ns	****
PDMS/PT	CTR						*	ns	****
	DIF							**	ns
PDMS/PA	CTR								****
	DIF								

Figure A.3: Statistical analysis of Quantification of Alizarin Red S concentration (μM) after 21 days. C: Undifferentiated control; D: Osteogenic Differentiation. Significance of the results is indicated according to P values with one, two, three or four of the symbols (*) corresponding to $0.01 \leq P < 0.05$; $0.001 \leq P < 0.01$; $0.0001 \leq P < 0.001$ and $P < 0.0001$, respectively; ns, not significant.